Available online at www.sciencedirect.com

ScienceDirect

Geochimica et Cosmochimica Acta 185 (2016) 251–277

Geochimica et Cosmochimica Acta

www.elsevier.com/locate/gca

Compositional heterogeneity of the Sugarloaf melilite nephelinite flow, Honolulu Volcanics, Hawai'i

David A. Clague [a,*], Frederick A. Frey [b], Michael O. Garcia [c], Shichun Huang [d], Michael McWilliams [e], Melvin H. Beeson [f]

[a] Monterey Bay Aquarium Research Institute, 7700 Sandholdt Road, Moss Landing, CA 95039, United States
[b] Department of Earth, Atmospheric and Planetary Sciences, Massachusetts Institute of Technology, United States
[c] Department of Geology and Geophysics, University of Hawai'i, Honolulu, HI, United States
[d] Department of Geoscience, University of Nevada Las Vegas, United States
[e] GNS Science, 1 Fairway Drive, Avalon 5010, PO Box 30-368, Lower Hutt 5040, New Zealand
[f] U.S. Geological Survey, Menlo Park, CA, United States

Available online 3 February 2016

Abstract

The Sugarloaf flow is a melilite nephelinite erupted from the Tantalus rift during rejuvenated-stage volcanism on O'ahu, the Honolulu Volcanics. The flow ponded in Mānoa Valley forming a ~15 m thick flow which was cored and sampled in a quarry. Nepheline from a pegmatoid segregation in the flow yielded a ^{40}Ar–^{39}Ar age of 76 ka. This age, combined with others, indicates that the Tantalus rift eruptions are some of the youngest on O'ahu. Honolulu Volcanics erupt on average about every 35–40 ka indicating that future eruptions are possible.

We evaluated the compositional variability of 19 samples from the flow, including 14 from the core. Twelve samples are representative of the bulk flow, four are dark- or light-colored variants, one is a heavy rare earth element (REE)-enriched pegmatoid, and two visually resemble the bulk flow, but have chemical characteristics of the dark and light variants. Our objective was to determine intraflow heterogeneity in mineralogy and composition. Variable abundances of Na_2O, K_2O, Sr, Ba, Rb, Pb and U in the flow were caused by post-eruptive mobility in a vapor phase, most likely during or soon after flow emplacement, and heterogeneous deposition of secondary calcite and zeolites. Relative to fine-grained samples, a pegmatoid vein that crosscuts the flow is enriched in incompatible trace elements except Sr and TiO_2. Element mobility after eruption introduced scatter in trace element ratios including light-REE/heavy-REE, and all ratios involving mobile elements K, Rb, Ba, Sr, Pb, and U. Lavas from some of the 37 Honolulu Volcanics vents have crosscutting REE patterns in a primitive mantle-normalized plot. Such patterns have been interpreted to reflect variable amounts of residual garnet during partial melting. Previous studies of lavas from different vents concluded that garnet, phlogopite, amphibole, and Fe–Ti oxides were residual phases of the partial melting processes that created the Honolulu Volcanics (Clague and Frey, 1982; Yang et al., 2003). However post-eruptive processes in the Sugarloaf flow also produced crossing REE patterns.

Eruptions on the Tantalus rift, including the Sugarloaf flow, produced volatile- and crystal-rich ash with interstitial glass and melt inclusions in olivine containing 4.2–6.4 wt% MgO compared to the flow average of 11.8 wt%. This flow erupted as a partially crystallized viscous magma at least 100 °C below its liquidus. The slow advance and cooling of the 15-m thick 'a' ā low promoted the segregation of pegmatoids, formation of light and dark bands with differing proportions of melilite and clinopyroxene, and induced volatile-enhanced mobility of incompatible elements.

* Corresponding author.
E-mail address: clague@mbari.org (D.A. Clague).

http://dx.doi.org/10.1016/j.gca.2016.01.034
0016-7037/

1. INTRODUCTION

Basalt is commonly used to probe planetary interiors. Radiogenic isotopic and trace element geochemistry are widely used to constrain the composition and mineralogy of the mantle sources of basalt (e.g., Gast, 1968; Hofmann, 2004). Basalts with broadly varying major and trace element compositions, but narrow ranges of radiogenic isotopic ratios, have been important in evaluating variations in melting processes (e.g., Frey et al., 1978). A prime example is the Honolulu Volcanics (HV) on O'ahu, Hawai'i (Fig. 1). Clague and Frey (1982) and Yang et al. (2003) inferred that the HV alkalic basalt, basanite, nephelinite, and melilite nephelinite lavas formed by 11–2% partial melting of a garnet lherzolite source, leaving residual phlogopite, amphibole, and a Ti-rich phase (perhaps an oxide), but not apatite. A marked depletion in K relative to elements of similar incompatibility in the highly alkaline HV lavas have been used to infer the presence of a K-rich phase in their mantle source (Clague and Frey, 1982; Class and Goldstein, 1997; Yang et al., 2003). The variable concentrations of some incompatible elements among HV lava and the anomalously low HREE concentrations in a single sample of the 15-m thick Sugarloaf flow led to concerns that post- or syn-eruptive intraflow processes may complicate the understanding of the petrogensisis of alkaline lavas.

Samples of the Sugarloaf flow, in common with other HV low-SiO_2 have high abundances of highly incompatible

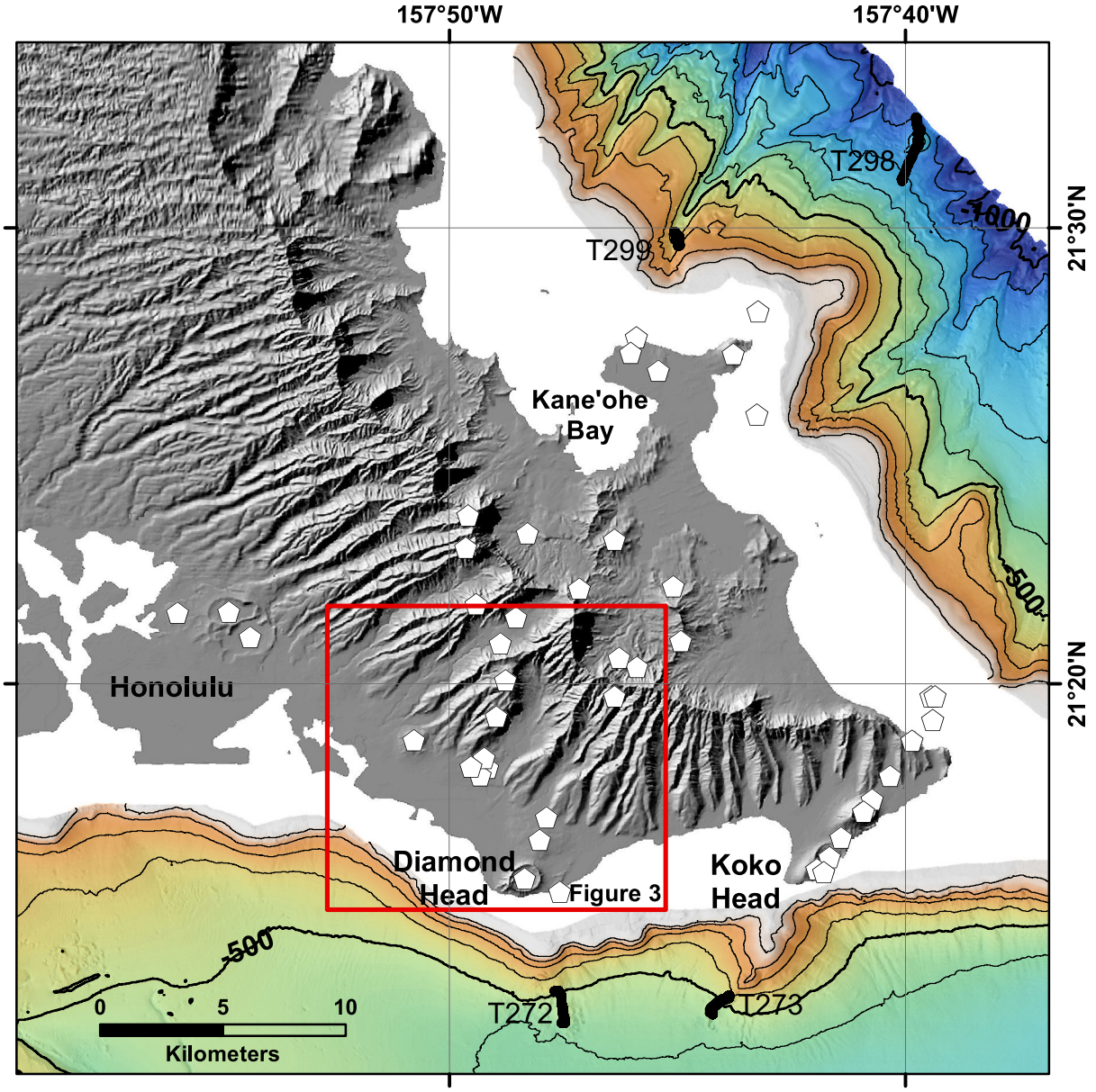

Fig. 1. Location map showing onshore and offshore vents of HV (Winchell, 1947). The box outlines the close-up map in Fig. 3. Offshore contours are 100 m. The labels T272, T273, T298, and T299 indicate submarine locations where HV lavas were sampled (Clague et al., 2006).

elements, e.g., Rb, Nb, and Ta (Clague and Frey, 1982; Yang et al., 2003). The Sugarloaf flow has the lowest SiO_2 content of all rejuvenated stage lavas in Hawai'i and the lowest concentrations of HREE (Tb to Lu), Y, and Sc (e.g., Sc and Lu are only 50% that in other HV flows, Fig. 2). Consequently, Yang et al. (2003) concluded that the mantle source of this flow had an unusually high proportion of garnet, a phase that preferentially incorporates HREE, Y, and Sc (e.g., Johnson, 1998). Fractionation of the HREE also occurred during segregation of pegmatoids within the flow. This study addresses the role of syn- and post-eruptive processes in modifying the composition of the Sugarloaf flow. Samples from this flow characteristic of the other low-SiO_2 HV flows (Clague and Frey, 1982; Yang et al., 2003).

During high lava fountain eruptions (Stearns and Vaksvik, 1935) the Sugarloaf and adjacent vents produced widespread >1 m thick cinder/ash deposits 6 km to the southwest in downtown Honolulu (ash locations on Fig. 1). Strongly SiO_2-undersaturated lavas, such as those from Nyiragongo Volcano (Tazieff, 1977; Tedesco et al., 2007), are notorious for their extremely rapid flow rates because of their low viscosities. Despite having lava composition similar to those erupted at Nyiragongo, the Sugarloaf eruption produced a 15-m thick a "ā" flow (Fig. 3; Stearns, 1940; Winchell, 1947). We evaluate why this eruption produced such high lava fountains, the cause of its high viscosity, and how the resulting flow was strongly affected by syn- and post-eruptive processes.

Another important parameter in assessing hazards is the long-term history of eruptions in the Honolulu area. The Sugarloaf flow is widely regarded as one of the youngest of the 37 clusters of HV vents (Winchell, 1947; Jackson and Wright, 1970; Ozawa et al., 2005). Nepheline separated from a pegmatoid in the Sugarloaf flow was dated using incremental ^{40}Ar–^{39}Ar to define the age and frequency of HV eruptions.

2. GEOLOGIC SETTING AND SAMPLES

The earliest geologists to visit O'ahu recognized the great unconformity that separates the HV from the underlying shield stage lavas of the Ko'olau Mountains (Dana, 1849; Dutton, 1884). The HV consist of the eruptive products from 37 named vents or groups of vents scattered widely over the southeastern part of O'ahu (Fig. 1). They were studied by Stearns and Vaksvik (1935, 1938), Stearns (1940), and Winchell (1947). Many of the HV lava flows, including the Sugarloaf flow described here, partly filled a valley cut up to 100 m into the underlying shield

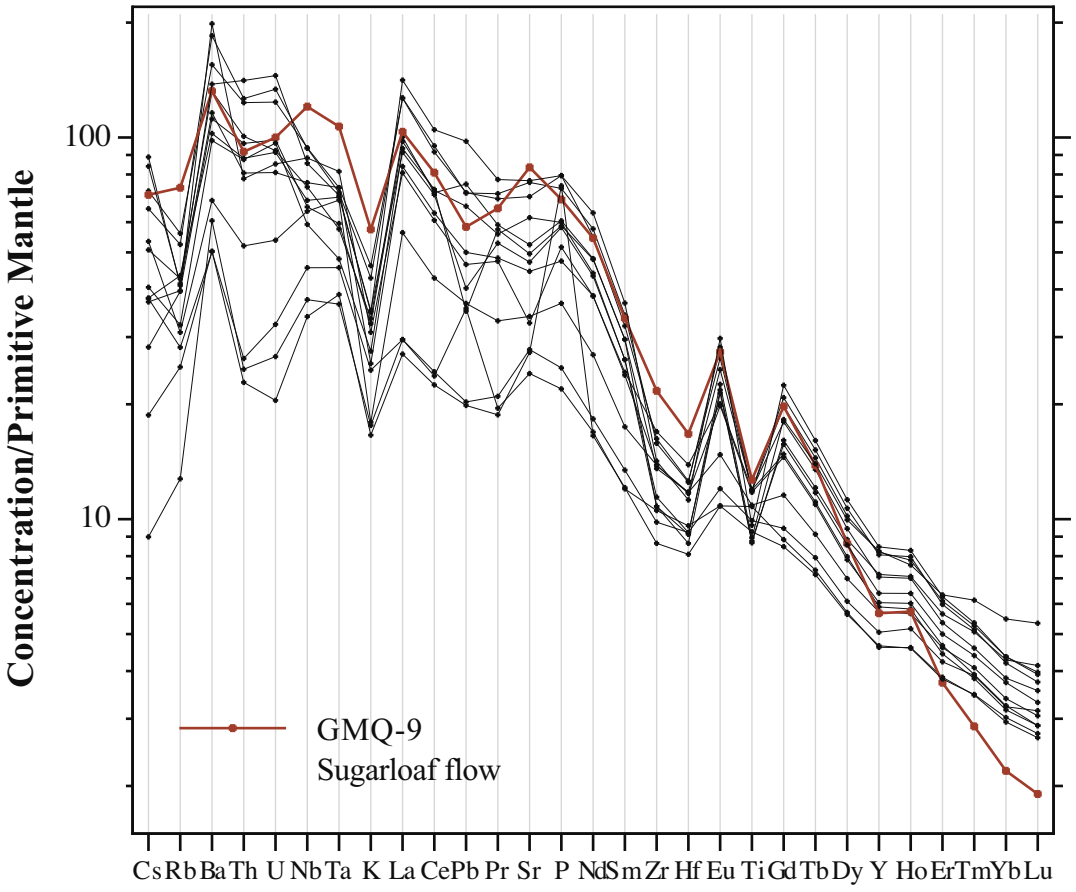

Fig. 2. Primitive mantle normalized HV lavas from Yang et al. (2003) showing the crossing pattern of the HREE of Sugarloaf flow sample GMQ9 in red. Elements are arranged with increasing incompatibility to the left using primitive mantle values from McDonough and Sun (1995).

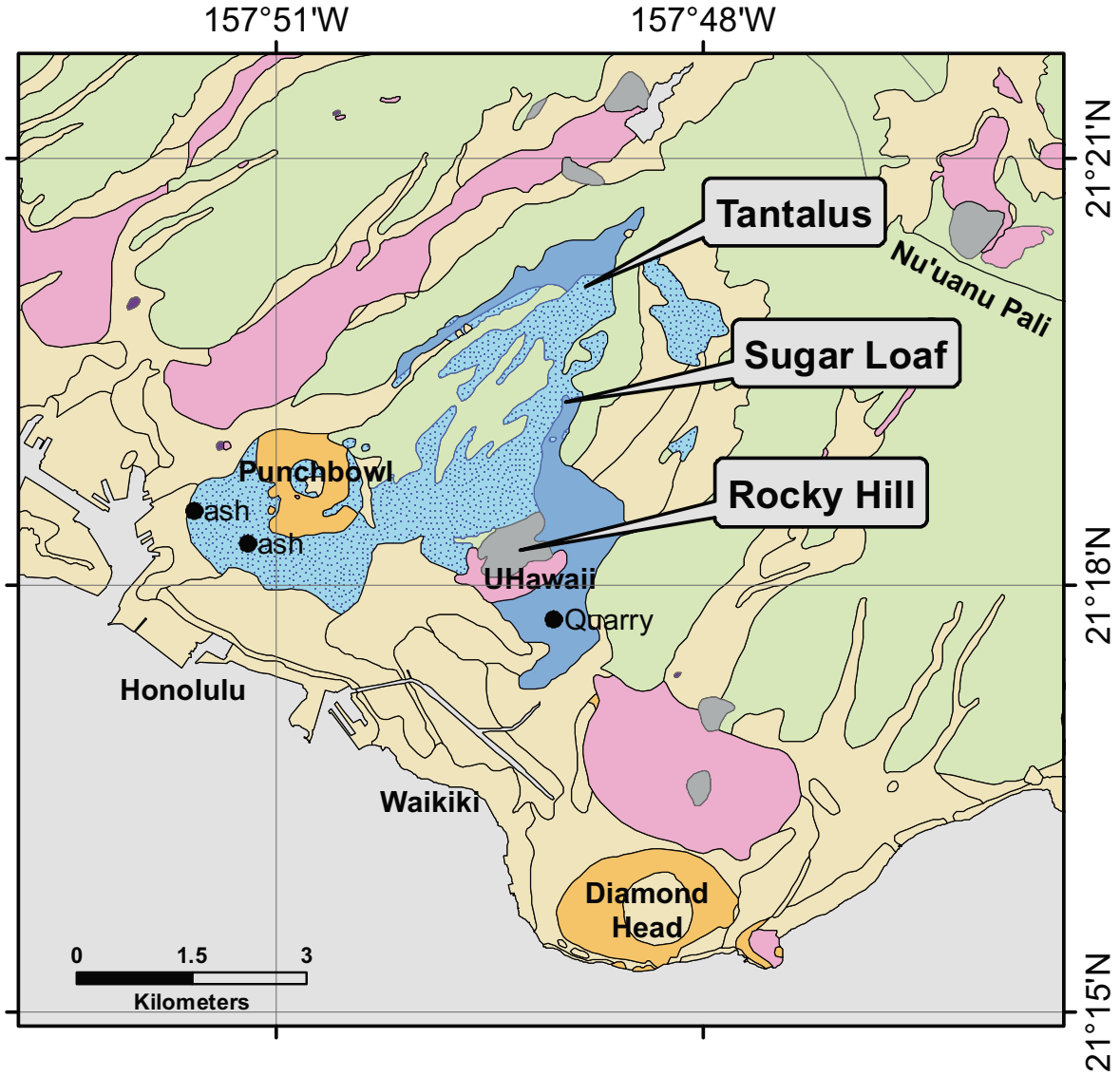

Fig. 3. Geologic map with Tantalus, Sugarloaf, and Rocky Hill indicating the vent locations of these related eruptions. Solid blue areas are lava flows and speckled blue areas are the known distribution of the ash erupted from the Tantalus rift. The quarry on the University of Hawaii campus is labeled, as are the locations of two ash samples. Pink areas indicate other flows, purple indicates vent deposits, and orange indicates ash cones in the HV. Green areas are flows of the underlying Koʻolau shield, and tan is sedimentary deposits.

lavas of Koʻolau Volcano. Clague and Dalrymple (1987) refer to these lavas as part of the rejuvenated stage. K–Ar dating confirms a hiatus in volcanic activity of about 1.4 Myr after the end of shield building (Makapuʻu-stage of Koʻolau) at 2.2 Ma to the start of the rejuvenated stage HV at ~800 ka (Gramlich et al., 1971; Laj et al., 2000; Ozawa et al., 2005; Yamasaki et al., 2011).

The HV consist of flows and tuffs with compositions ranging from melilite nephelinite, nephelinite, basanite, and weakly alkalic basalt (Winchell, 1947; Clague and Frey, 1982). The Sugarloaf flow is one of the youngest and most SiO_2-undersaturated of all rejuvenated stage lavas in Hawaiʻi (Winchell, 1947). The flow originated from Puʻu Kākea and Round Top vents on a ridge west of Mānoa Valley (Sugarloaf on Fig. 3; Stearns, 1940). The mineral compositions of the lava and its pegmatoid segregations were described by Wilkinson and Stolz (1983). The Sugarloaf flow has been sampled numerous times (Hitchcock, 1900; Cross, 1915; Tilley et al., 1965; Schilling and Winchester, 1969; Jackson and Wright, 1970; Philpotts et al., 1972; Clague and Frey, 1982; Wilkinson and Stolz, 1983; Yang et al., 2003), in part because it is readily accessible in the Mōʻiliʻili quarry wall on the University of Hawaii campus (quarry on Fig. 3).

We obtained a 14.2 m core through the Sugarloaf flow that provides a nearly complete cross section. The core was drilled 0.9 km from the distal end of the flow and about 20 m from the face of the Mōʻiliʻili quarry as part of a foundation study for the University of Hawaii Law School. We evaluated the compositional variation and heterogeneity of

Table 1
Major element analyses of Sugarloaf flow.

Sample	Uniform samples														
	GMQ1	GMQ2	GMQ3	GMQ4	GMQ5	GMQ6	GMQ7	GMQ7.5	GMQ8	GMQ9	GMQ11	65MOIL2	Mean	StDev	%Dev
Depth	**0.91** m	**3.14**	**4.94**	**5.94**	**6.13**	**7.92**	**9.30**	**10.06**	**10.82**	**11.95**	**13.14**				
SiO_2	35.7	36.8	36.0	35.9	36.1	35.6	35.9	36.9	35.3	36.5	36.0	35.52			
TiO_2	2.66	2.79	2.68	2.74	2.73	2.66	2.75	2.64	2.64	2.75	2.70	2.78			
Al_2O_3	10.0	10.6	10.3	10.2	10.1	10.2	10.4	10.2	10.1	9.94	10.2	11.01			
Fe_2O_3	8.63	10.19	8.04	8.90	9.01	11.37	6.73	16.60	10.88	8.00	7.52	9.82			
FeO	7.53	6.84	8.24	7.74	7.16	4.80	9.60	0.00	5.33	8.28	8.62	7.13			
MnO	0.23	0.24	0.23	0.24	0.24	0.23	0.24	0.25	0.23	0.23	0.24	0.25			
MgO	12.1	11.3	11.6	11.6	11.1	11	11.5	11	11.3	11.4	11.5	11.46			
CaO	11.5	10.1	12.6	12.4	13	13.4	12.5	13.2	13.6	12.9	12.5	12.17			
Na_2O	4.54	5.14	5.03	4.69	3.84	4.26	5.15	4.30	3.79	4.80	4.56	4.84			
K_2O	1.57	1.86	1.80	1.77	1.69	1.52	1.79	1.40	1.17	1.73	1.67	1.72			
P_2O_5	1.05	1.20	1.13	1.14	1.17	1.14	1.16	1.12	1.13	1.16	1.15	1.05			
H_2O^+	1.36	0.24	1.23	0.91	1.54	1.58	0.32	2.17	1.65	0.75	0.83	0.58			
H_2O^-	0.95	0.91	0.59	0.78	1.55	1.06	0.38	-	1.36	0.71	0.86	0.63			
CO_2	0.79	0.09	0.24	0.20	0.17	0.13	0.17	0.23	0.19	0.16	0.13	0.26			
S, F, Cl	0.56	1.21	-	0.30	0.30	0.39	0.36	-	0.60	0.57	0.34	1.38			
Total	99.17	99.51	99.71	99.51	99.73	99.34	98.95	99.01	99.47	99.68	98.8	99.34			
Normalized to 100%															
SiO_2	37.72	38.32	37.17	37.23	37.90	37.46	36.99	38.46	37.40	37.67	37.54	36.71	37.55	0.51	1.39
TiO_2	2.81	2.91	2.77	2.84	2.87	2.80	2.83	2.75	2.80	2.84	2.82	2.87	2.82	0.04	1.54
Al_2O_3	10.57	11.04	10.64	10.58	10.60	10.73	10.72	10.63	10.70	10.26	10.64	11.38	10.71	0.27	2.40
FeO^*	16.16	16.67	15.98	16.33	16.03	15.82	16.13	15.57	16.02	15.98	16.04	16.50	16.10	0.29	1.78
MnO	0.24	0.25	0.24	0.25	0.25	0.24	0.25	0.26	0.24	0.24	0.25	0.26	0.25	0.01	2.84
MgO	12.78	11.77	11.98	12.03	11.65	11.57	11.85	11.46	11.97	11.77	11.99	11.84	11.89	0.33	2.81
CaO	12.15	10.52	13.01	12.86	13.65	14.10	12.88	13.76	14.41	13.31	13.03	12.58	13.02	1.02	8.09
Na_2O	4.80	5.35	5.19	4.86	4.03	4.48	5.31	4.48	4.02	4.95	4.75	5.00	4.77	0.45	8.91
K_2O	1.66	1.94	1.86	1.84	1.77	1.60	1.84	1.46	1.24	1.79	1.74	1.78	1.71	0.20	11.02
P2O5	1.11	1.25	1.17	1.18	1.23	1.20	1.20	1.17	1.20	1.20	1.20	1.09	1.18	0.05	4.22

(*continued on next page*)

Table 1 (*continued*)

Sample	HREE Depleted				Light colored			Dark colored			Pegmatoid	
	GMQ12	GMQ12/Mean	MQ1	MQ1/Mean	GMQ10L	MQ2L	Light/Mean	GMQ10D	MQ2D	Dark/Mean	PEG	PEG/Mean
Depth	**14.08**				**12.83**			**12.83 m**				
SiO_2	35.5		36.4		36.3	35.8		36.0	37.2		41.5	
TiO_2	2.87		2.86		2.70	2.82		2.69	2.87		3.03	
Al_2O_3	9.87		10.7		9.75	10.6		9.75	10.5		11.9	
Fe_2O_3	10.75		6.36		8.21	6.60		8.89	6.55		4.95	
FeO	6.34		10.35		8.36	10.75		7.57	10.66		8.05	
MnO	0.23		0.23		0.24	0.25		0.24	0.26		0.25	
MgO	11.2		10.56		12.3	11.1		14.3	15.3		5.26	
CaO	13.3		13.1		12.2	12.7		8.47	8.42		13.0	
Na_2O	5.09		5.25		4.32	4.94		3.81	3.93		5.99	
K_2O	1.83		1.91		1.57	1.90		1.56	1.77		2.87	
P_2O_5	1.11		1.12		1.10	1.11		1.12	1.15		2.06	
H_2O^+	0.39		0.49		1.15	2.18		2.16	0.46		1.66	
H_2O^-	0.21		–		0.99	-		2.34	-		-	
CO_2	1.38		0.38		0.24	0.45		0.25	0.13		0.28	
S,F, Cl	0.36		0.67		0.24	0.61		0.69	0.61		0.61	
Total	100.43		99.62		99.83	101.2		99.84	99.15		100.81	
Normalized to 100%												
SiO_2	36.59	0.975	37.09	0.988	37.72	36.52	0.989	38.50	37.98	1.018	42.20	**1.124**
TiO_2	2.96	1.047	2.91	1.032	2.81	2.88	1.006	2.88	2.93	1.028	3.08	**1.090**
Al_2O_3	10.17	0.950	10.86	1.015	10.13	10.82	0.978	10.43	10.74	0.989	12.06	**1.126**
FeO^*	16.51	1.025	16.38	1.017	16.37	17.05	1.037	16.65	16.90	1.042	12.71	**0.789**
MnO	0.24	0.958	0.23	**0.947**	0.25	0.26	1.019	0.26	0.27	1.055	0.25	1.027
MgO	11.54	0.971	10.76	**0.905**	12.78	11.38	1.016	15.29	15.58	**1.298**	5.35	**0.450**
CaO	13.71	1.053	13.31	1.022	12.68	12.98	0.985	9.06	8.60	**0.678**	13.26	1.018
Na_2O	5.25	**1.100**	5.35	**1.122**	4.49	5.05	1.000	4.07	4.01	**0.848**	6.09	1.277
K_2O	1.89	**1.104**	1.95	**1.139**	1.63	1.94	1.045	1.67	1.81	1.017	2.92	1.707
P_2O_5	1.14	0.968	1.14	0.966	1.14	1.13	0.964	1.20	1.17	1.004	2.09	1.772

Bold font indicates high variability or significant differences.

Table 2
Trace element analyses by X-ray fluorescence spectrometry, instuemental neutron activation, isotope dilution.

	Uniform samples														
	GMQ1	GMQ2	GMQ3	GMQ4	GMQ5	GMQ6	GMQ7	GMQ7.5	GMQ8	GMQ9	GMQ11	65MOIL2	Mean	StDev	% Var.
XRF															
Rb	41	47	50	50	54	46	48	41	38	49	48	51	46.9	4.7	**10.0**
Sr	1512	1260	1723	1709	1728	1974	1716	1759	2322	1799	2186	1550	1770	287	**16.2**
Ba	932	569	899	904	901	909	929	800	1007	881	937	940	884	110	**12.4**
V	249	236	235	231	223	193	240		227	229	232	230	230	14.0	6.1
Ni	220	245	202	231	209	201	209	262	182	206	208	230	217	21.8	**10.0**
Zn	208	206	193	190	180	182	200	173	184	195	198	175	190	11.6	6.1
Ga	22.4	24.4	23.0	21.9	19.9	23.2	25.6	21.6	25.1	22.5	23.1		23.0	1.6	7.1
Y	22.5	24.0	22.2	23.2	22.8	23.1	23.6	22.2	22.2	22.4	23.4		22.9	0.6	2.8
Zr	240	250	235	245	244	236	249	288	237	237	253	240	246	14.5	5.9
Nb	84	85	78	84	81	77	84	108	78	79	84		83.8	8.6	**10.2**
INAA															
Sc	14.3	15.8	15.2				15.8	14.7	14.6		14.8	13.6	14.9	0.7	5.0
Cr	347	375	364				357	341	331		340	326	348	16.7	4.8
Co	71.1	76.2	73.1				74.5	71.5	70		72.7	75	73.0	2.1	2.9
Hf	4.7	5.4	4.9				5.3	4.7	4.9		5.2	5.3	5.1	0.3	5.6
Ta	3.9	4.3	3.9				4.1	4.0	4.0		4.2	4.6	4.1	0.2	5.8
Th	7.2	8.1	7.7				8.2	7.5	7.4		7.9	7.9	7.7	0.4	**4.5**
La	65.7	70.6	69.6				71.8	69.2	68.0		70.0	73.0	69.7	2.2	3.2
Ce	141	148	148				152	147	147		151	146	148	3.3	2.3
Nd	65	68.4	68.5				70.2	68	69.1		69.7	66	68.1	1.8	2.6
Sm	13.4	15.0	14.8				15.4	14.5	14.4		14.6	15.4	14.7	0.6	4.4
Eu	4.59	4.86	4.62				4.80	4.60	4.65		4.72	4.70	4.69	0.10	2.1
Tb	1.51	1.42	1.31				1.33	1.49	1.40		1.42	1.50	1.42	0.08	5.3
Yb	0.89	0.92	0.95				1.03	0.75	0.98		0.92	1.20	0.96	0.13	**13.4**
Lu	0.14	0.16	0.12				0.14	0.13	0.12		0.13	0.14	0.14	0.01	9.7
ID															
Cs							0.71			0.63			0.7	0.1	8.4
Sr							1707						1707		
Rb							43.9			47.1			45.5	2.3	5.0
Ba							876			945			910.5	48.8	5.4

(*continued on next page*)

Table 2 (*continued*)

	HREE Depleted				Light colored			Dark Colored			Pegmatoid	
	GMQ12	GMQ12/Mean	MQ1	MQ1/Mean	GMQ10L	MQ2L	Light/Mean	GMQ10D	MQ2D	Dark/Mean	PEG	PEG/Mean
XRF												
Rb	46	0.980	45	0.959	42	54	1.023	43	48	0.970	74	**1.577**
Sr	1596	**0.902**	1806	1.020	2315	2376	**1.325**	1439	1070	**0.709**	1733	0.979
Ba	734	**0.830**	740	**0.837**	1034	760	1.015	974	1150	1.201	2380	**2.692**
V	225	0.980	252	1.098	236	263	**1.087**	224	230	0.989	249	**1.085**
Ni	210	0.967	173	**0.797**	233	160	**0.905**	218	185	0.928	27	**0.124**
Zn	190	0.998	197	1.035	207	209	**1.093**	206	218	**1.114**	186	0.977
Ga	24.0	1.045	25.4	1.106	22.6	26.4	1.066	23.4	27.3	**1.103**	24.0	**1.045**
Y			21.9	0.957	21.9	22.3	0.966	22.4	23.4	1.001	50.6	**2.212**
Zr	226	**0.918**	234	0.951	244	245	0.993	245	244	0.993	616	**2.502**
Nb	69	**0.823**	79	0.943	84	82	0.990	84	91	1.044	211	**2.517**
INAA												
Sc	13.1	**0.882**	14.6	0.983	13.7	13.5	**0.916**	14.1	14.1	0.949	37	**2.492**
Cr	284	**0.817**	344	0.990	346	337	0.982	342	329	0.965	6	**0.017**
Co	72.3	0.990	80	1.096	72.6	76	1.018	71.8	75	1.005	34.1	**0.467**
Hf	4.7	0.931	5.4	1.069	4.8	5.6	1.030	4.9	5.1	0.990	13	**2.574**
Ta	3.7	**0.899**	4.3	1.042	4.2	4.6	1.070	4.2	4.7	1.075	9.8	**2.376**
Th	6.0	0.775	8.0	1.034	7.7	7.4	0.976	7.5		0.969	19.2	**2.481**
La	61.6	**0.883**	69.6	0.998	65.0	74.2	0.998	64.2	75.6	1.002	130.0	**1.864**
Ce	134	**0.908**	146	0.990	140	142	0.956	141	157	1.010	268	**1.817**
Nd	62.7	**0.921**	66	0.969	65.3	64	0.949	64.9	69	0.983	118	**1.732**
Sm	13.0	**0.885**	14.7	1.001	13.2	15.3	0.970	13.4	15.5	0.984	27.0	**1.838**
Eu	4.40	**0.938**	4.65	0.991	4.49	4.81	0.991	4.46	4.97	1.005	8.42	**1.794**
Tb	1.33	**0.935**	1.71	**1.202**	1.32	1.56	1.012	1.42	1.48	1.019	2.88	**2.025**
Yb	0.69	**0.723**	1.26	**1.319**	0.94	1.11	1.073	0.94	1.26	**1.152**	2.74	**2.869**
Lu	0.11	**0.815**	0.13	0.963	0.13	0.14	1.000	0.13	0.16	**1.074**	0.36	**2.667**
ID												
Cs					0.70							
Sr						2780					1731	
Rb					40.6	59.4					71.7	
Ba					1034							

MQ2L and PEG ID data for Sr and Rb from Roden et al. (1984). Bold font indicates high variability or significant differences.

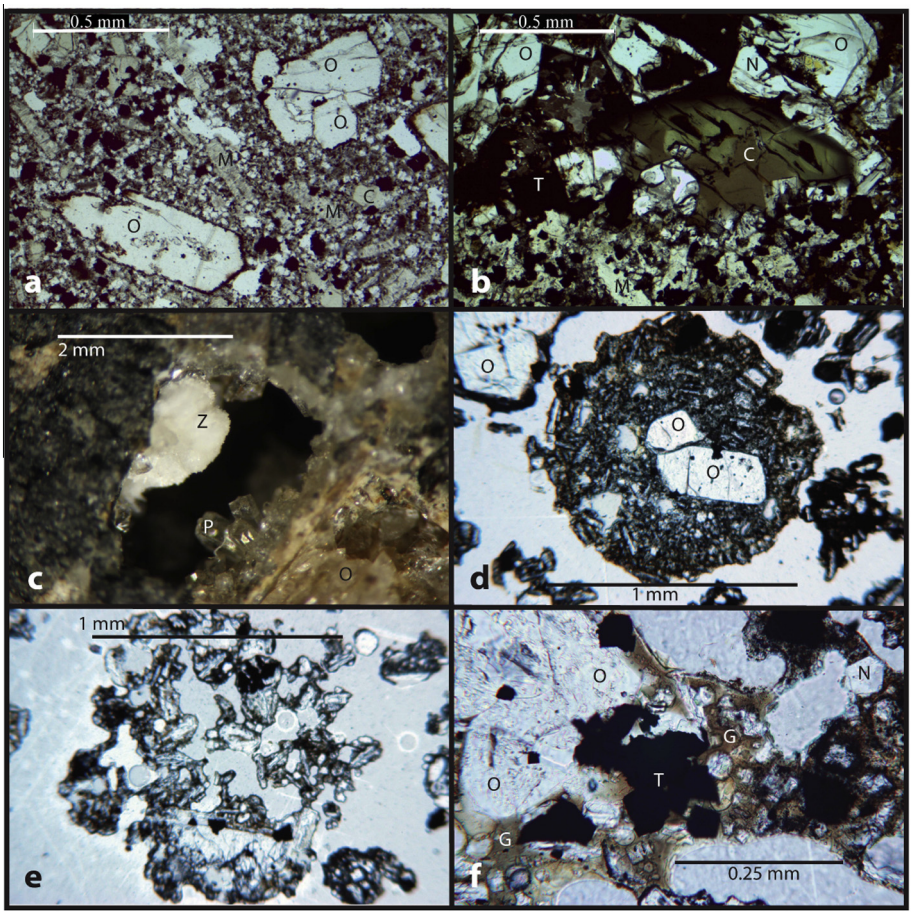

Fig. 4. Photomicrographs of lava from the Sugarloaf flow and lapilli from the Tantalus ash. Panel (a) shows the texture the melilite nephelinite flow with microphenocrysts of 0.5 mm olivine (O), lath-shaped melilite (M), and blocky clinopyroxene (C). The finer matrix contains melilite, clinopyroxene, nepheline, titanomagnetite, and rare sodalite. Panel (b) shows the sharp contact between the pegmatoid (top) and the finer-grained flow (bottom). Olivine (O), clinopyroxene (C), titanomagnetite (T), and nepheline (N) are labeled in the pegmatoid. Panel (c) shows a zeolite lined vug in the pegmatoid. Most of the zeolite is clear euhedral phillipsite, with less abundant radiating fibrous white zeolite that may be natrolite or stilbite. Panels (d) and (e) show two examples of rounded nearly holocrystalline lapilli from the Tantalus ash. Panel (f) shows rare reddish-brown interstitial glass in lapilli from the Tantalus ash (Table 4).

the flow and determined the within-flow compositional variation using samples from the core and five additional samples from the quarry face.

Nearby vents Rocky Hill and Tantalus (Fig. 3) have variable melilite contents, but similar compositions (Fekiakova et al., 2007) and ages (Ozawa et al., 2005) to the Sugarloaf flow and have been inferred to erupt along a single rift (Ozawa et al., 2005) although Rocky Hill was not included as part of the Tantalus Rift by Stearns and Vaksvik (1935), Winchell (1947), or Jackson and Wright (1970). An extensive ~1–2 m thick ash deposit extends at least 6 km southwest of the vents to downtown Honolulu (Stearns and Vaksvik, 1935; Winchell, 1947) is interpreted as lava fountain deposits produced during simultaneous eruptions at the Sugarloaf and Tantalus vents (Stearns and Vaksvik, 1935). We analyzed two samples of this ash (TAN1 and TAN2) recovered during excavations near the intersection of Beretania and Ala Streets and the intersection between Alakea and South Hotel Streets (ash on Fig. 3). The ash at these sites is about 1 m thick, directly overlies the 123 ± 2 ka old Waim ānalo limestone (McMurtry et al., 2010), and underlies about 1 m of soil.

3. ANALYTICAL TECHNIQUES

Much of the analytical work was done in the 1980s, mostly in laboratories at the U.S. Geological Survey. Major oxides were analyzed by X-ray fluorescence (XRF) (J.S. Wahlberg, J. Taggart, and J. Baker in the X-ray Spectroscopy Project in Lakewood, Colorado using techniques described by Taggart et al. (1987)). Classical chemical techniques were used to analyze H_2O^+, H_2O^-, CO_2, and FeO (S. Seeley, N. Neiman, G. Nason, and E. Engleman of the Rock Analysis Project in Lakewood, Colorado).

Some trace elements were analyzed by XRF (H. Rose, R. Johnson, J. Rose, B. McCall, G. Sellers, and J. Lindsay in the X-ray Spectroscopy Project in Reston, Virginia). A few samples (GMQ7, GMQ9, and GMQ10L were analyzed by XRF for trace and major elements at the University of Massachusetts, Amherst. Trace elements (Table 2) were

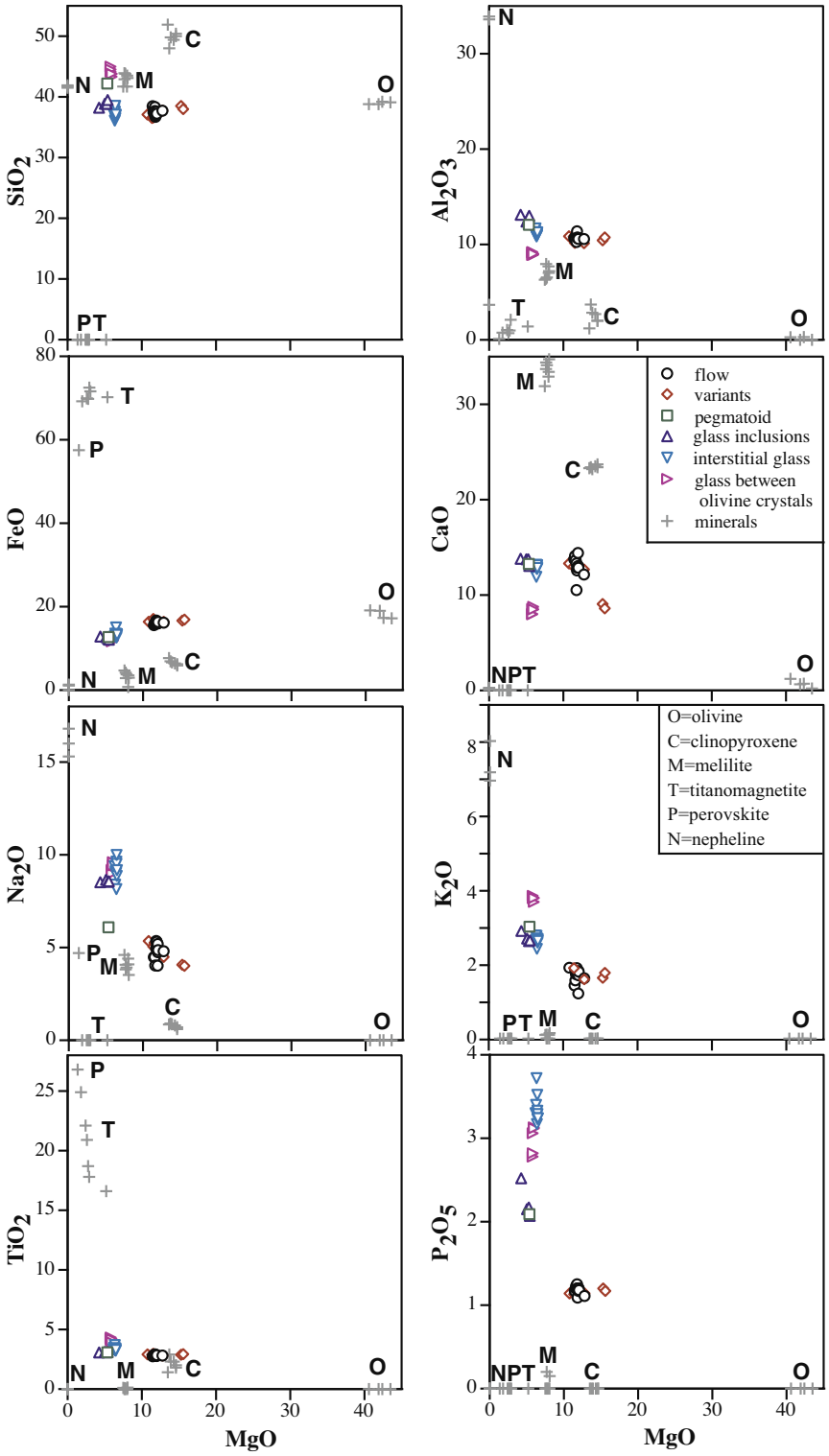

Fig. 5. MgO-variation diagrams showing the 19 samples from the Sugarloaf flow (Table 1) and glass inclusions, interstitial glasses, and clean glass between olivine crystals in the ash samples (Table 4). Mineral compositions for olivine (O), clinopyroxene (C), melilite (M), titanomagntite (T), nepheline (N), and perovskite (P) from Wilkinson and Stolz (1983) and Appendix 1.

also analyzed by Instrumental Neutron Activation Analysis (INAA) at MIT, using techniques described in Ila and Frey (1984). A subset of samples was analyzed for Sr, Nd, Sm, and Rb by isotope dilution at MIT (Roden et al., 1984).

In order to obtain a more precise data set, the entire sample suite was analyzed by inductively-coupled plasma mass spectrometry (ICP-MS) at Harvard University. About 0.05 g rock powder was digested at 120 °C for a week using

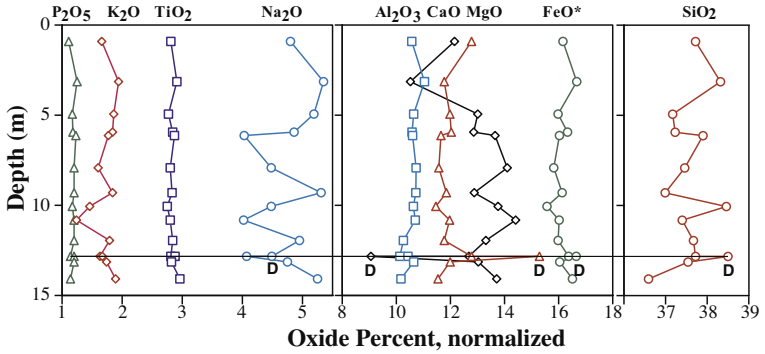

Fig. 6. Major oxides vs depth in core showing variability in most oxides, but particularly in CaO, Na_2O and to a smaller degree K_2O. Dark variants (D) of sample GMQ10 are labeled and indicated by light horizontal line.

1:1 mixed concentrated HF and concentrated HNO_3 in 4 ml Telfon beakers. The samples were dried with concentrated HNO_3 three times to remove HF and were then diluted using 5% HNO_3 with a dilution factor of 5000 for ICP-MS measurement. The diluted solutions were measured on a Thermo X series quadrupole ICP-MS. One solution of USGS rock standard BHVO-1 was measured every 5 samples to monitor the sensitivity drift. Solutions of USGS standards BHVO-1, AGV-1 and BCR-1 were used to construct the calibration curves, and Sr, whose abundances were available by XRF, was used as an internal standard. Basalt rock standard BHVO-2 was measured as an unknown.

Ash samples were analyzed by electron microprobe at the U.S. Geological Survey in Menlo Park, CA on a JEOL Superprobe using natural and synthetic glass and mineral standards as described by Davis et al. (1994) using Smithsonian Juan de Fuca glass VG2 as the standard for SiO_2, Al_2O_3, FeO^*, MgO, CaO and Na_2O.

A nepheline separate from a Sugarloaf flow pegmatoid vein, with ~8wt% K_2O (Wilkinson and Stolz, 1983), was dated by step heating ^{40}Ar–^{39}Ar at Stanford University in a Heine-design double vacuum resistance furnace. The extracted gases were purified using SAES Zr–Al getters and released into a Mass Analyzer Products 216 model mass spectrometer with Baur-Signer ion source and an electron multiplier. Mass discrimination in the spectrometer was monitored by measuring purified air before and after the step heating experiments, yielding an average $^{40}Ar/^{36}Ar$ ratio of 292.6 ± 1.5.

4. RESULTS

4.1. Core description

Drilling penetrated 14.17 m and recovered 11.84 m of core (83.5% recovery). The uppermost 0.61 m was not recovered, and the next 1.52 m is heavily fractured dark gray, vesicular aphanitic basalt (Fig. 4a). The surfaces of fractures are Fe-oxide or caliche stained to 4.08 m depth. A zeolite-rich vuggy section, with a coarse, almost diabasic texture, occurs from 5.18 to ~7.3 m depth. Starting at ~8 m depth, vesicles are rare, although zeolites persist to the base of the core. Grain size is finer below ~10 m depth. Pegmatoid veins ((Fig. 4b) are present in the core at 6.71, 9.20, 9.60, 10.06, 12.95 and 13.53 m depths; the lower two veins have glassy margins. Fourteen core samples were selected for analysis, including adjacent samples, one lighter colored (GMQ10L) than the other (GMQ10D).

4.2. Mō'ili'ili quarry

The quarry face shows features similar to the core, although some pegmatoid veins are up to 0.3 m thick, especially near the middle of the exposed quarry section. The flow contains 2–3 m wide vertical columnar joints. Several samples from the lower part of the quarry face labeled MQ1 and MQ2 were also analyzed, with both light and dark variants for sample MQ2. Our study included a sample from a thick pegmatoid vein (PEG). Sample 65MOIL2 (Jackson and Wright, 1970; Clague and Frey, 1982) collected near the base of the exposed outcrop in the quarry wall, was included in this study.

4.3. Petrography of core and quarry face samples

The Sugarloaf flow is a melilite nephelinite (Fig. 4b) that contains 13–21 vol% olivine microphenocrysts with small enclosed Cr-spinel, 19–29 vol% melilite microphenocrysts, 10–23 vol% nepheline, 13–19 vol% clinopyroxene, 17–23 vol% opaque oxides, a trace to ~2 vol% apatite, a trace of blue sodalite (based on 7.8–8% Cl in analyses in Wilkinson and Stolz, 1983), a trace of perovskite (U. Hawaii microprobe analysis, Appendix 1) and 3–8 vol% fine unidentified material (perhaps altered glass) normalized on a vesicle-, zeolite-, and calcite-free basis. Vesicles are abundant near the top (14 vol%) and decrease to 2 vol% near the base. Calcite is present at trace amounts except in sample GMQ12, which contains 3 vol%. Zeolite (phillipsite and chabazite; Dunham, 1933) filled vesicles are abundant near the top of the flow (maximum 7 vol% in GMQ4) and decrease to trace amounts near the base of the core. Melilite occurs in two forms, one (in GMQ2) altered to a gray, fine-grained material with ribbon or peg structures and a second (in GMQ4, GMQ7, GMQ8, GMQ11, and GMQ12) that is slightly pleochroic with higher birefringence

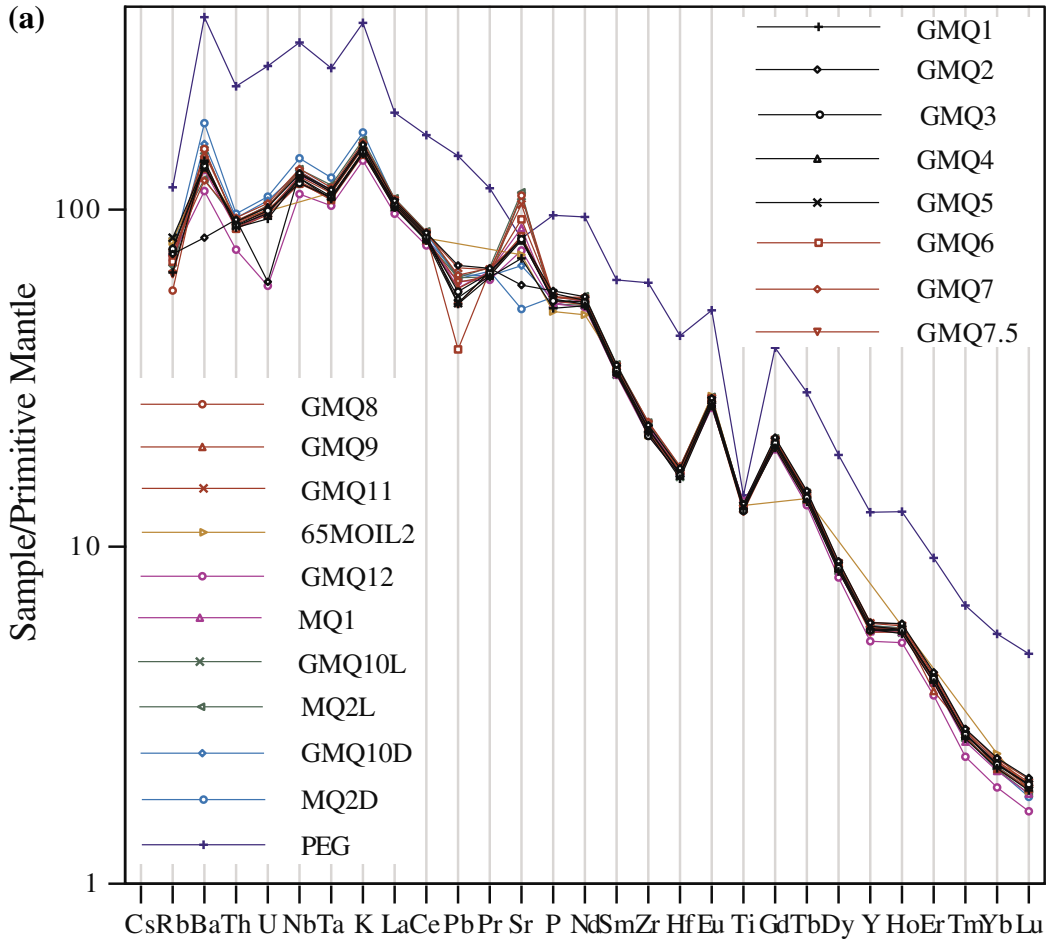

Fig. 7. (a) Primitive mantle normalized plot for all Sugarloaf samples using primitive mantle values from McDonough and Sun (1995). Most samples are similar with the exception of the pegmatoid. Samples from the upper 7 m of flow in black, lower 7 m of flow in red, light variants in green, dark variants in cyan, and pegmatoid in lavender. (b) Ratios of 12 main samples representative of the bulk flow normalized to the mean of the same 12 samples. Elements arranged as in primitive mantle normalized plots by decreasing incompatibility. Most elements have small variability in abundance except Rb, Ba, U, Pb, and Sr. Sr is enriched in the lower flow samples and depleted in the upper flow samples. (c). The standard deviation of the 12 samples plotted in (b) showing that the abundances of all elements vary by at least twice the analytical precision, with large variability in Cs, Rb, Ba, U, K, Pb, and Sr.

rims (yellowish) than the first type. The light and dark GMQ10 variants differ mainly in the much greater percentage of melilite (26% vs 13.5%) and lower percentage of opaque Fe-oxides (12 vs 19 vol%) in the light variant.

4.4. Mineral compositions

Wilkinson and Stolz (1983) presented mineral compositions for olivine, clinopyroxene, melilite, titanomagnetite, nepheline, and sodalite from a pegmatoid zone and a fine-grained flow sample. We analyzed these phases, except sodalite, by electron microprobe at the University of Hawaii (Appendix 1); the compositions agree with their data and both data sets are plotted in Fig. 5. Small red-brown perovskite crystals contain ~27.0% TiO_2, 57.5% FeO^*, 0.75% MnO, 1.35% MgO, and 4.5–5% Na_2O (Appendix 1). Some melilite grains are strongly zoned in SrO ranging from 0.9% to 1% in the cores to 2.8% in the rims (Appendix 1). Melilite with high SrO contents and strongly zoned to SrO-rich rims also occur in nephelinites from the Camroons (Fitton and Hughes, 1981) The SrO rich rims were not found on melilite in the pegmatoid. Zeolites (Fig. 4c) include phillipsite and chabazite (Dunham, 1933). Some phillipsite(?) has elevated Ba contents.

4.5. Whole-rock chemical composition of Sugarloaf samples

We divided the Sugarloaf samples into 4 groups based on visual and chemical criteria. We refer to a group of 12 samples (Table 1) as the main samples, because they are representative of the bulk flow composition. The other 7 samples are grouped by their special characteristics, that is, two that are light-colored, and two that are dark-colored, two that are visually identical to 11 samples from the core and 65MOIL2 but are HREE-depleted, and one pegmatoid.

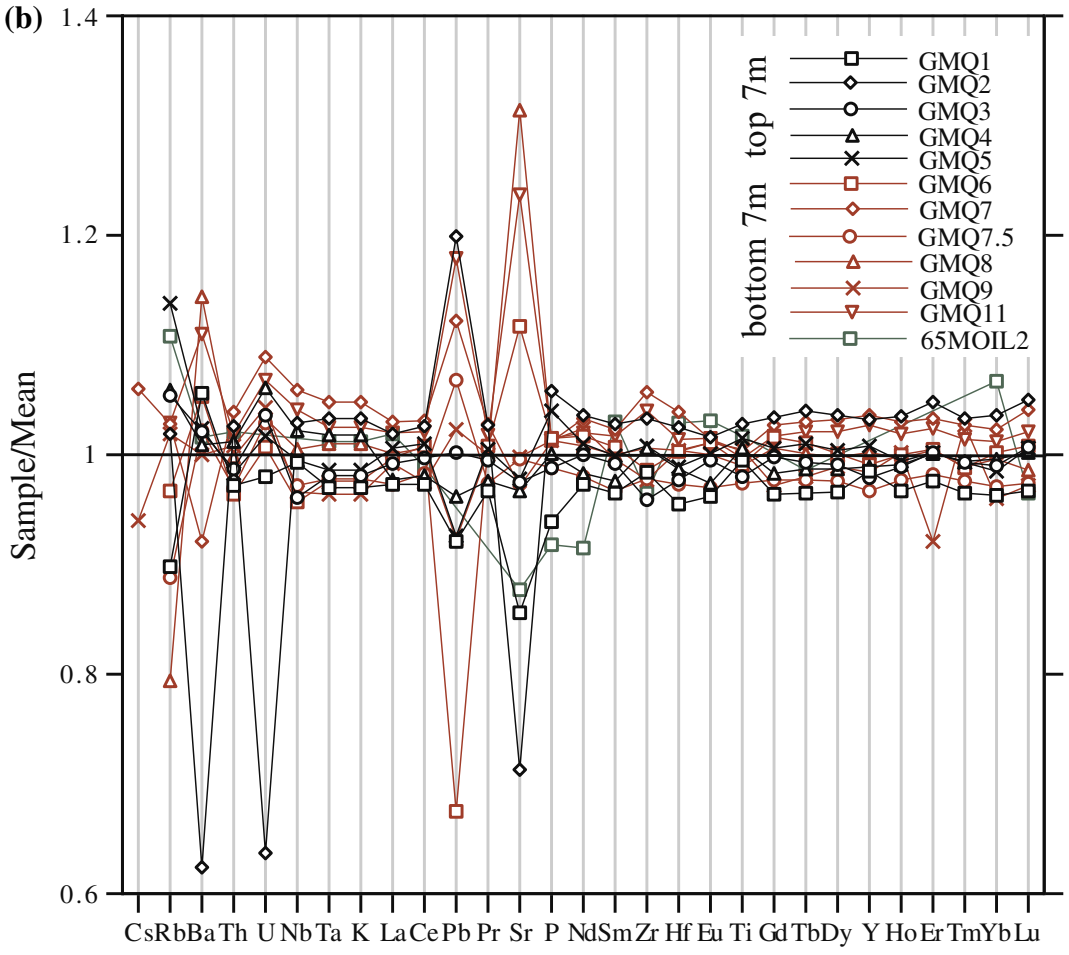

Fig 7. *(continued)*

4.5.1. Major element compositions

Abundances of Na_2O, K_2O, and CaO vary widely with depth in the core (Fig. 6), but SiO_2, FeO^*, P_2O_5, and TiO_2 are nearly constant (Table 1). MgO and Al_2O_3 are constant through much of the core, but the top sample and dark and light variants near the base vary significantly from the mean (mean and standard deviation for the 12 main samples, and the ratios of oxides in all the variants to the mean of the main samples are in Table 1). The dry, reduced normalized concentrations for the 12 main samples show that most major element oxides are relatively homogenous (% deviation from the mean is <3.7%) except for CaO, Na_2O, and K_2O, which deviate from their mean values by 7%, 9%, and 11%, respectively. The two light colored variants are not significantly different from the main parts of the flow, whereas the two dark-colored variants are 31% higher in MgO and 23% and 16% lower in CaO and Na_2O than the main samples. The pegmatoid varies significantly from the main samples in all oxides except MnO and CaO. P_2O_5, K_2O and SiO_2 are 78%, 68% and 13% higher, respectively, in the pegmatoid whereas MgO and FeO^* are 55% and 21% lower. All the samples are plotted on MgO-variation diagrams in Fig. 5 with microprobe compositions of the minerals in the flow.

4.5.2. Trace element compositions

The 19 samples from the flow are shown on a primitive mantle-normalized plot (Fig. 7a) that shows that, relative to the other 18 samples, the pegmatoid is enriched in all incompatible elements except Sr and Ti. In order to illustrate subtle geochemical differences each of the 12 main samples is normalized to the mean of the 12 samples (Fig. 7b). Among the main samples, most incompatible trace elements vary by 2–4%, generally slightly greater than the analytical precision (Fig. 7c, Tables 2 and 3). Abundances of the commonly mobile incompatible elements Ba, U, K, Pb, and Sr, and to a lesser degree Cs and Rb, are much more variable (12–15%, 8–10% for Cs and Rb) than their analytical precision (~3%). There are systematic differences with depth in the core (e.g., Sr is systematically higher in the middle to lower portions of the core, except for the base, which is similar to the flow top; Fig. 8a). Abundances of transition series metals (Sc, V, Cr, Co, Ni, Zn) are relatively homogeneous in the core with deviations from the mean < 6.1% except for Ni, which varies by 10% and Cr, which has lower abundance in the lowermost sample GMQ12 (Fig. 8b).

The two light-colored variants (GMQ10L and MQ2L) differ significantly from the main samples: Sr, Pb, V, Zn,

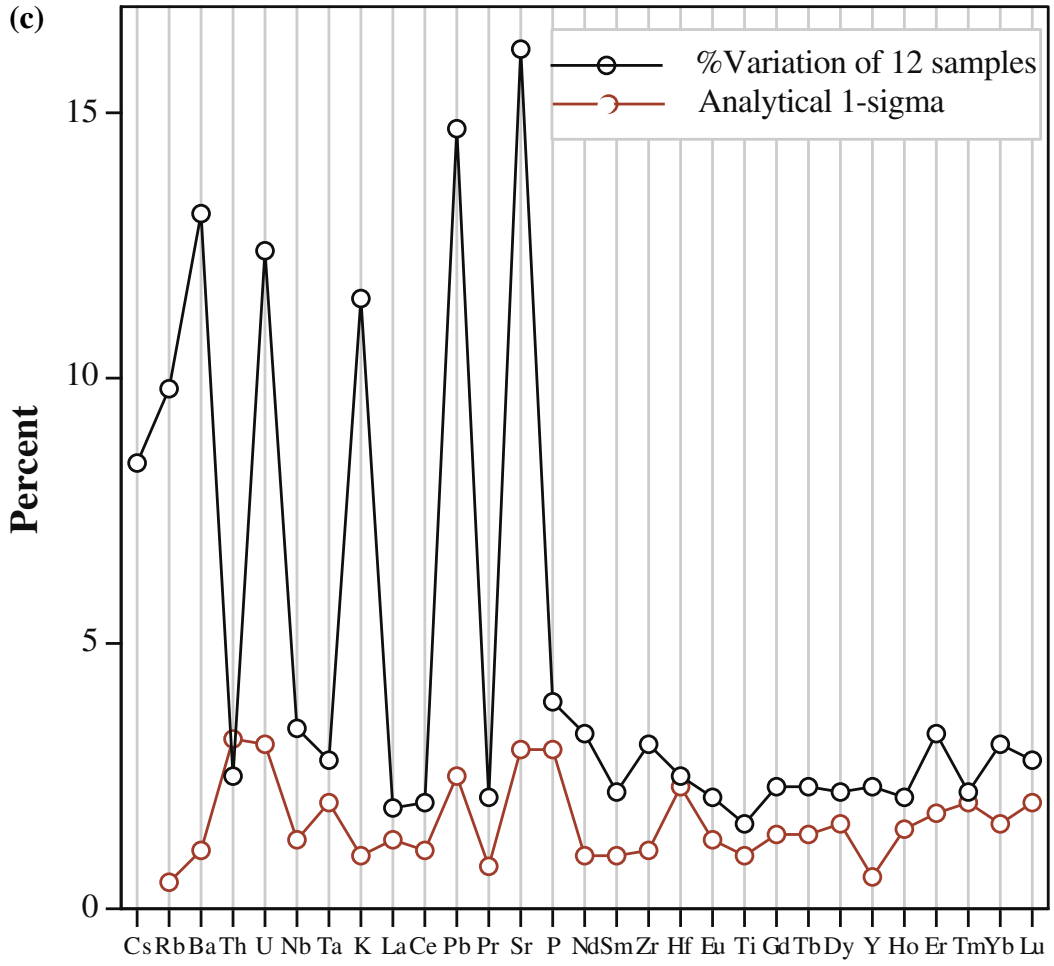

Fig 7. *(continued)*

U, are 33%, 10%, 9%, 9%, and 7% higher and Ni and Sc are 10 and 8% lower than the mean of the main samples (Tables 2 and 3). The dark-colored variants (GMQ10D and MQ2D in Fig. 7) also differ significantly from the main samples with Sr 29% lower, and Ba, U, Pb, Nb, Ta, and Th higher by 27%, 13%, 11%, 9%, 8%, and 5%, respectively, relative to the mean of the 12 main samples (Tables 2 and 3). The dark and light variants (Fig. 9) have elevated abundances of highly incompatible elements compared to the mean of the main samples, but the most notable difference is the Sr enrichment in the light variants and depletion in dark variants.

Samples from near the base of the flow (GMQ12 and MQ1), despite their visual similarity to the main samples, have compositional characteristics that set them apart from the main group. GMQ12, in particular, has lower HREE (with the HREEs depleted by about 16% from the mean of the main flow samples). Consequently the REE pattern for GMQ12 crosses the Sugarloaf main samples at Gd (Fig. 9). Relative to the mean of the main samples this sample has low abundances of highly incompatible elements, high TiO_2, and low Cr. Sample MQ1 shares some of these same characteristics, but to a much lesser degree (Fig. 9); MQ1D, MQ1L, MQ2, and GMQ12 share the characteristic of being 4–16% depleted in HREE relative to the mean of the main samples; and GMQ10D and GMQ10L differ less from the mean than the other variant samples.

The pegmatoid differs from the mean of the main samples in all elements except Sr and Ti, with other incompatible elements enriched by 160–280% compared with the main flow (Fig. 10). Ba, Th, Pb, Zr, Hf, and the HREE are the most enriched with lower enrichments for Rb, K, LREE, and P. HREE are more enriched (250%) than LREE (~180%). The pegmatoid has a small positive Ce anomaly as Ce is slightly more enriched than either La or Pr. It is also highly depleted, as noted by Wilkinson and Stolz (1983), in compatible elements Ni, Cr, and Co by 88%, 98%, and 53% relative to the main flow mean.

There are also large variations in ratios of these mobile elements in the core (Fig. 11). For example, K/Ba ranges from ~9 to 27 and Ba/Rb ~12 to 29 compared to Sm/Yb of ~13 with the basal sample GMQ12 at 15. The pegmatoid sample has Ba/Rb of 35 and Sm/Yb of 10.

4.6. Petrography of ash samples

The mineralogy of the two ash samples from downtown Honolulu, olivine microphenocrysts, melilite, clinopyroxene,

Table 3
ICPMS trace element analyses.

Sample	Representative samples														
	GMQ1	GMQ2	GMQ3	GMQ4	GMQ5	GMQ6	GMQ7	GMQ7.5	GMQ8	GMQ9*	GMQ11	65MOIL2#	Mean	StDev	% var.
Sr-XRF	1512	1260	1723	1709	1728	1974	1716	1759	2322	1763	2186	1550	1767	287	16.2
Sc	14.99	15.85	14.89	14.49	15.00	15.49	15.48	14.74	15.12		15.03	13.6	14.97	0.59	3.9
Rb	41.3	46.9	48.5	48.7	52.4	44.5	47.3	40.9	36.5	46.9	47.3	51	46.03	4.52	9.8
Zr	245	257	239	250	251	245	263	243	250	243	259	240	249	7.7	3.1
Y	25.8	27.1	25.7	25.9	26.4	26.0	27.2	25.4	26.3	25.8	26.9		26.22	0.61	2.3
Nb	88.2	91.5	85.4	90.8	88.4	85.1	94.1	86.4	89.3	85.9	92.5		88.9	3.1	3.4
Ba	977	577	944	933	947	974	852	945	1058	925	1027	940	925	121.1	13.1
La	69.7	73.0	71.1	70.0	72.1	71.5	73.8	69.7	71.7	71.1	73.1	73.0	71.7	1.40	1.9
Ce	144	152	147	145	149	149	152	145	149	144	151	146	148	2.96	2.0
Pr	17.4	18.5	17.9	17.6	18.1	18.1	18.5	17.5	18.0	18.0	18.3		18.0	0.37	2.1
Nd	70.2	74.7	72.1	70.9	72.8	73.3	74.5	70.7	72.7	73.8	73.6	66.0	72.1	2.41	3.3
Sm	14.4	15.4	14.8	14.6	14.9	15.1	15.3	14.5	15.0	14.9	15.2	15.4	15.0	0.33	2.2
Eu	4.39	4.63	4.53	4.44	4.56	4.61	4.62	4.42	4.56	4.61	4.63	4.7	4.56	0.10	2.1
Gd	11.7	12.6	12.1	11.9	12.2	12.3	12.5	11.9	12.2	11.8	12.3		12.1	0.28	2.3
Tb	1.47	1.58	1.51	1.50	1.54	1.54	1.57	1.49	1.52	1.49	1.55	1.5	1.52	0.03	2.3
Dy	6.22	6.67	6.38	6.35	6.46	6.44	6.65	6.28	6.43	6.37	6.57		6.44	0.14	2.2
Ho	0.906	0.970	0.926	0.928	0.931	0.937	0.965	0.915	0.934	0.939	0.954		0.937	0.020	2.1
Er	1.90	2.04	1.95	1.95	1.95	1.95	2.01	1.91	1.95	1.79	1.99		1.94	0.07	3.3
Tm	0.20	0.21	0.20	0.21	0.20	0.20	0.21	0.20	0.20	0.21	0.21		0.21	0.00	2.2
Yb	1.08	1.17	1.11	1.12	1.11	1.13	1.15	1.09	1.12	1.08	1.14	1.2	1.13	0.04	3.1
Lu	0.140	0.152	0.146	0.145	0.146	0.146	0.151	0.141	0.143	0.141	0.148	0.14	0.145	0.004	2.8
Hf	4.92	5.28	5.03	5.08	5.10	5.17	5.35	5.01	5.17	5.17	5.22	5.3	5.15	0.13	2.5
Ta	4.41	4.70	4.46	4.63	4.48	4.44	4.76	4.45	4.59	4.38	4.66	4.6	4.55	0.13	2.8
Pb	3.73	4.85	4.05	3.89	3.75	2.73	4.54	4.32	3.74	4.14	4.77		4.05	0.59	**14.7**
Th	7.52	7.94	7.64	7.83	7.60	7.46	8.04	7.51	7.72	7.80	7.88	7.9	7.74	0.19	2.5
U	1.97	1.28	2.08	2.14	2.05	2.03	2.19	2.07	2.08	2.10	2.15		2.01	0.25	**12.4**

(*continued on next page*)

Table 3 (*continued*)

Sample	HREE Depleted				Light colored			Dark colored			Pegmatoid	
	GMQ12	GMQ12/Mean	MQ1	MQ1/Mean	GMQ10L	MQ2L	Light/Mean	MQ2D	GMQ10D	Dark/Mean	PEG	PEG/Mean
Sr-XRF	1596	**0.903**	1860	1.053	2315	2376	**1.328**	1070	1439	**0.710**	1733	0.98
Sc	14.0	0.933	14.4	0.960	14.0	13.6	**0.920**	12.9	14.5	**0.918**	39.5	**2.64**
Rb	46.4	1.008	45.8	0.995	42.4	52.3	1.029	46.9	43.6	0.983	74.0	**1.61**
Zr	239	0.962	253	1.019	249	262	1.026	256	255	1.027	680	**2.73**
Y	23.8	**0.909**	25.5	0.974	25.7	26.5	0.996	26.5	26.1	1.004	57.6	**2.20**
Nb	79.3	**0.892**	90.1	1.014	91.4	94.0	1.043	101.3	92.6	**1.090**	223	**2.51**
Ba	793	**0.858**	918	0.992	1048	860	1.032	1262	1095	**1.274**	2602	**2.81**
La	66.8	0.932	71.4	0.997	69.5	74.2	1.003	73.4	70.3	1.003	133	**1.86**
Ce	139	0.941	148	1.000	143	153	1.003	151	145	1.003	295	**2.00**
Pr	17.1	0.949	18.1	1.006	17.4	18.6	1.001	18.1	17.5	0.991	31.9	**1.77**
Nd	69.5	0.964	73.3	1.017	70.4	75.0	1.008	72.8	70.9	0.997	129	**1.79**
Sm	14.3	0.959	15.0	1.004	14.4	15.4	0.997	15.0	14.6	0.990	27.5	**1.84**
Eu	4.34	0.951	4.55	0.998	4.40	4.68	0.996	4.63	4.48	0.999	8.44	**1.85**
Gd	11.6	0.954	12.2	1.004	11.7	12.5	0.998	12.2	12.0	0.998	23.2	**1.91**
Tb	1.43	0.942	1.52	0.999	1.48	1.56	0.999	1.54	1.50	1.000	3.10	**2.04**
Dy	5.97	**0.928**	6.35	0.986	6.25	6.58	0.996	6.49	6.37	0.999	13.8	**2.14**
Ho	0.851	**0.909**	0.915	0.977	0.912	0.941	0.989	0.939	0.930	0.998	2.08	**2.22**
Er	1.74	**0.895**	1.89	0.974	1.91	1.95	0.994	1.94	1.96	1.003	4.45	**2.29**
Tm	0.18	**0.854**	0.20	0.945	0.20	0.20	0.976	0.20	0.21	0.993	0.50	**2.40**
Yb	0.95	**0.844**	1.06	0.946	1.10	1.08	0.968	1.07	1.12	0.976	2.72	**2.42**
Lu	0.122	**0.839**	0.137	0.944	0.141	0.137	0.959	0.134	0.144	0.960	0.356	**2.45**
Hf	5.06	**0.982**	5.22	1.013	4.98	5.33	1.001	5.01	5.14	0.985	13.1	**2.53**
Ta	4.21	**0.926**	4.68	1.029	4.63	4.85	1.043	5.10	4.69	**1.077**	10.8	**2.37**
Pb	4.35	**1.074**	4.16	1.028	4.46	4.46	**1.103**	4.43	4.55	**1.110**	10.2	**2.53**
Th	6.47	**0.836**	7.48	0.967	7.83	7.81	1.011	8.26	8.03	**1.053**	19.7	**2.55**
U	1.25	**0.620**	2.05	1.017	2.16	2.13	**1.066**	2.29	2.23	**1.125**	5.60	**2.78**

(*continued on next page*)

Table 3 (*continued*)

	Standard as unknown			USGS recommended	
Sample	BHVO-2	StDev	% var.	BHVO-2	StDev
Sr-XRF	399			389	23
Sc	33.5	0.613	1.8	32	1
Rb	9.50	0.051	0.5	9.8	1.0
Zr	175	1.841	1.1	172	11
Y	28.4	0.169	0.6	26	2
Nb	19.9	0.253	1.3	18	2
Ba	132	1.487	1.1	130	13
La	15.2	0.195	1.3	15	1
Ce	37.6	0.422	1.1	38	2
Pr	5.48	0.042	0.8		
Nd	24.8	0.246	1.0	25.0	1.8
Sm	6.15	0.062	1.0	6.2	0.4
Eu	1.98	0.026	1.3		
Gd	6.07	0.083	1.4	6.3	0.2
Tb	0.94	0.013	1.4	0.9	
Dy	5.27	0.086	1.6		
Ho	0.99	0.015	1.5	1.04	0.04
Er	2.49	0.044	1.8		
Tm	0.34	0.007	2.0		
Yb	1.99	0.032	1.6	2.0	0.2
Lu	0.28	0.006	2.0	0.28	0.01
Hf	4.39	0.099	2.3	4.1	0.3
Ta	1.33	0.027	2.0	1.4	
Pb	1.37	0.034	2.5		
Th	1.22	0.039	3.2	1.2	0.3
U	0.42	0.013	3.1		

Bold font indicates high variability or significant differences.

[*] Yang et al. (2003).

[#] Clague and Frey (1982).

titanomagnetite, nepheline, and fine-grained unidentified material, is similar to that of the Sugarloaf flow. Ash lapilli are commonly rounded (Fig. 4d and e) and highly vesicular. Interstitial glass is rare (Fig. 4f) and reddish-brown in color.

4.6.1. Composition of glass in ash samples

Glasses of two different compositions and locations occurs in the lapilli, in addition to a third composition present as glass inclusions in some olivine crystals (TAN1 and TAN2 in Table 4). The melt inclusions have lower MgO and FeO*, higher Al_2O_3 and TiO_2, but much higher Na_2O, K_2O, and P_2O_5 than the Sugarloaf lava samples (Tables 1 and 4, Fig. 5). The glass inclusion and intergranular groundmass glass compositions are remarkable in their high Cl and S contents, both >2600 ppm. The second type of groundmass glass occurs as small crystal-free patches within clusters of olivine microphenocrysts; these intra-phenocryst glasses have higher SiO_2 and TiO_2, much higher Na_2O, K_2O and P_2O_5, and lower MgO, FeO*, Cl, and S than the glass inclusions or intergranular glasses. The glass inclusions and intergranular glasses have SiO_2 similar to the bulk Sugarloaf flow, but the intra-phenocryst glasses have higher SiO_2. The three types of glasses all have extraordinary high Na_2O contents > 8%, K_2O > 2.6%, P_2O_5 > 2%, and Cl > 2600 ppm, much lower MgO contents than the Sugarloaf flow samples (4.9–6.3 vs ~12 wt%, and are plotted with the 19 Sugarloaf flow samples on expanded MgO-variation diagrams (Fig. 5) that include mineral compositional data (Wilkinson and Stolz, 1983; and Appendix 1). All three types of glass are distinct from the main Sugarloaf flow or pegmatoid compositions, although the glass inclusions are most similar to the pegmatoid.

4.7. Age of Sugarloaf flow

Nepheline was separated from a pegmatoid sample and dated using incremental ^{40}Ar–^{39}Ar technique (Table 5). The nepheline from the flow and pegmatoid contains ~8 wt% K_2O (Wilkinson and Stolz, 1983) and is therefore similar in K_2O content to volcanic sanidine used to date many ash flows. A six-step analysis yielded consistent total fusion, plateau, and inverse isochron ages (Fig. 12) of 76 ± 1, 76 ± 1, and 76 ± 2 ka at 1-sigma level, respectively. This 76 ± 1 ka age is the most precise date for any HV flow and is similar to previous dates obtained for the Sugarloaf flow (67 and 90 ka; Gramlich et al., 1971; Ozawa et al., 2005). All three ages are consistent with the stratigraphic position of the ash from the eruptions from the Tantalus rift on top of the Waim ānalo limestone, dated at 123 ± 2 ka (McMurtry et al., 2010).

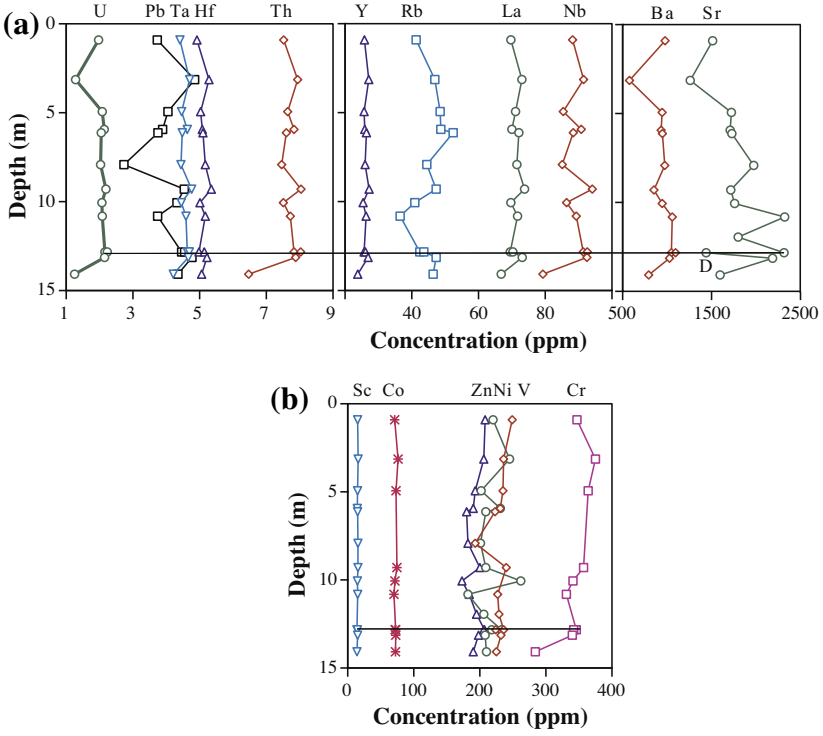

Fig. 8. (a) Abundances of incompatible trace elements (U, Pb, Ta, Hf, Th, Y, Rb, La, Nb, Ba, and Sr) vs depth in the core. Rb, Ba, Sr, U, and Pb contents vary significantly, with Ta, Hf, and La constant and Th, Y, and Nb constant except in the lowermost sample GMQ12. Light and dark variants of GMQ10 are the same except that Sr abundance is lower than in the dark variant. Some of this variability was used to identify GMQ12 (basal sample) as a variant. (b) Compatible trace element abundances vs depth in the core. Sc and Co contents are homogeneous through the core; those of Zn and V are slightly more heterogeneous, and Ni contents are the most variable. Cr abundance is constant except the basal sample GMQ12 which has low Cr.

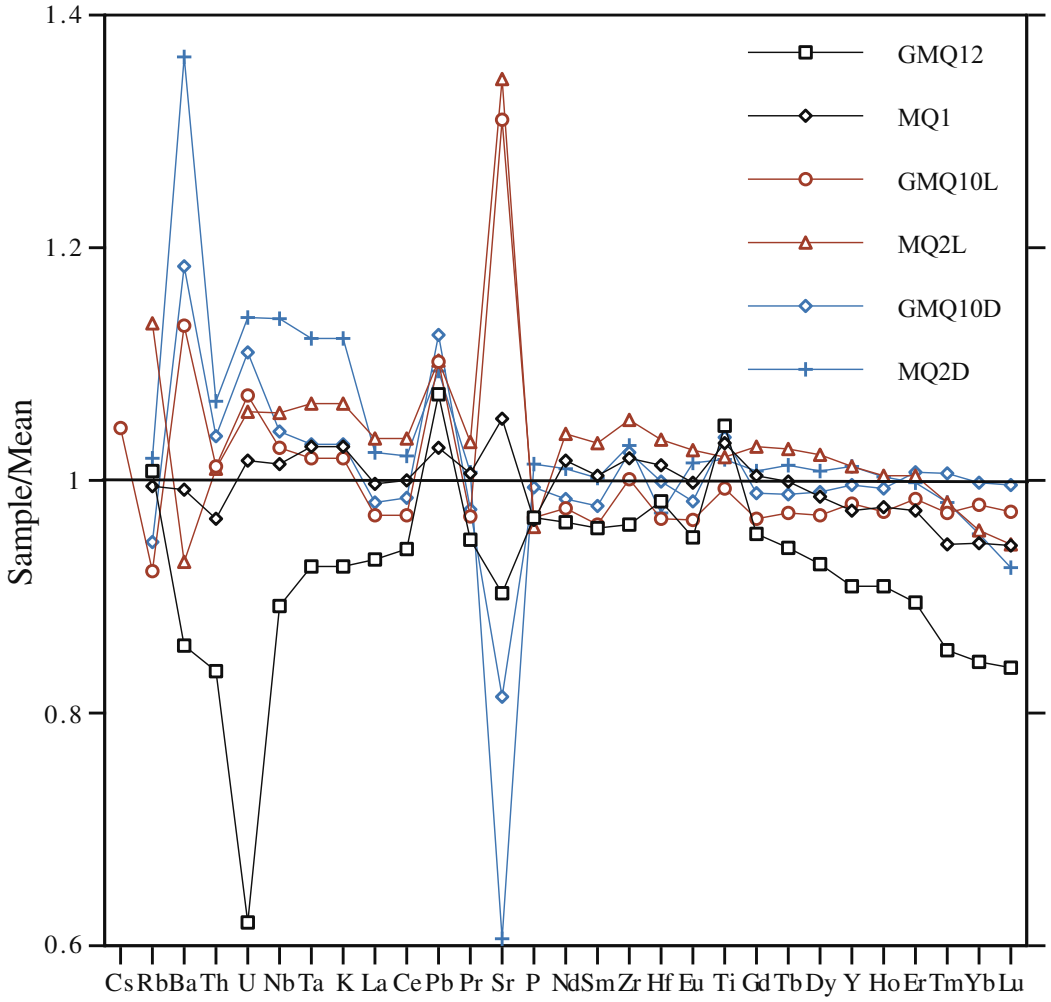

Fig. 9. Abundances of light (GMQ10L and MQ2L), dark (GMQ10D and MG2D), and HREE-enriched (GMQ12 and MQ1) variants normalized to the mean of 12 main flow samples. Most variants are slightly depleted in HREE and slightly enriched in elements more incompatible than La. Light variants are enriched in Sr whereas dark ones are depleted in Sr and enriched in Ba. GMQ12 is depleted in HREE and U.

5. DISCUSSION

5.1. Compositional variability in the Sugarloaf flow

The intraflow variations in major and trace elements (Tables 1–3) show that the Sugarloaf flow is heterogeneous in chemical composition. Consequently analysis of one sample that is not representative of the bulk flow could lead to erroneous interpretations about the origin of the magma that formed this flow. The composition of the Sugarloaf flow was affected by at least three post-partial melting processes. The first and most obvious is element mobility during crystallization that led to large variations of Rb, Ba, U, K, Pb, and Sr within the flow (Figs. 8b, 9 and 10). This variability was likely caused by volatile transport of these elements and heterogeneous deposition of secondary minerals such as zeolites and calcite either during the last stages of crystallization or during subsequent post-magmatic alteration. Abundances of these elements are also highly variable in thick flows of tholeiitic basalt that form the shields of Hawai'ian volcanoes (Huang et al., 2016) where the variability is attributed to abundance of olivine phenocryst and low-temperature processes such as leaching and alteration. The much greater variability of these elements in the Sugarloaf flow than in the shield tholeiites, and the zeolites in vugs and vesicles was likely caused by volatile transport of these elements and their heterogeneous deposition during the last stages of crystallization.

Segregation of late stage melt to form pegmatoid veins has also created compositional heterogeneity within the Sugarloaf flow (Fig. 10). Segregation of even a modest amount of pegmatoid would deplete the remaining flow in all incompatible elements except for Sr and Ti, and increase abundances of transition metals such as Ni, Cr, and Co, and the ratio of LREE/HREE in the remaining flow (Fig. 10).

A third process that created heterogeneity was formation of the light and dark variants in the flow with the Sr-rich light variants containing more melilite and less clinopyroxene and

Table 4
Microprobe analyses of glass in Tantalus ash.

Sample	SiO_2	TiO_2	Al_2O_3	FeO*	MnO	MgO	CaO	Na_2O	K_2O	P_2O_5	Cl	S	Total
Inclusions													
Tan2-GC1a*	37.7	3.03	12.9	12.6	0.31	4.17	13.6	8.40	2.92	2.48	0.368	0.360	98.5
Tan2-GC1e*	38.4	3.08	12.3	12.6	0.24	4.96	13.6	8.55	2.72	2.13	0.284	0.294	98.9
Tan2-GC1f*	38.4	3.05	12.6	12.2	0.26	5.21	13.6	8.45	2.65	2.15	0.266	0.284	98.9
Tan2-GC1 g*	39.0	3.06	12.8	11.9	0.23	5.34	12.9	8.46	2.67	2.04	0.264	0.268	98.7
Average*	38.4	3.06	12.7	12.3	0.26	4.92	13.4	8.47	2.74	2.20	0.296	0.301	98.8
Interstitial Glass													
Tan1-RC1a*	36.6	3.36	11.0	13.5	0.35	6.45	12.8	10.01	2.65	3.30	0.343	0.313	100.2
Tan1-RC1b*	36.8	3.25	11.0	13.0	0.33	6.41	13.1	9.62	2.75	3.33	0.355	0.328	99.9
Tan1-RC2c*	36.8	3.26	11.2	13.2	0.37	6.43	12.7	9.09	2.67	3.21	0.354	0.316	99.2
Tan1-RC2d*	36.6	3.39	11.0	13.1	0.37	6.38	12.7	9.44	2.69	3.21	0.358	0.326	99.3
Tan1-RC4a*	35.8	3.66	11.2	14.9	0.37	6.30	11.8	9.08	2.45	3.14	0.453	0.380	99.2
Tan1-RC4b*	38.2	3.34	11.0	12.8	0.35	6.32	12.8	9.13	2.72	3.31	0.325	0.331	100.3
Tan1-RC2e*	36.6	3.19	11.1	13.3	0.37	6.40	13.0	8.77	2.70	3.21	0.363	0.317	99.0
Tan1-RC4c	38.2	3.38	10.9	12.5	0.31	6.36	12.9	8.08	2.73	3.49	0.321	0.350	99.1
Tan2-RC2a*	37.0	3.24	10.9	12.8	0.37	6.22	12.5	8.90	2.79	3.67	0.284	0.260	98.6
Tan2-RC2b*	36.8	3.23	10.6	12.7	0.34	6.25	12.9	8.85	2.69	3.22	0.357	0.357	98.1
Tan2-RC3a*	36.8	3.30	11.3	12.7	0.29	6.10	12.6	9.28	2.81	3.26	0.345	0.320	98.9
Tan2-RC3b	36.9	3.43	11.6	13.4	0.30	6.20	12.5	8.32	2.69	3.37	0.424	0.371	99.2
Average*	36.8	3.33	11.1	13.2	0.35	6.32	12.7	9.14	2.69	3.29	0.360	0.329	99.2
Glass between olivine crystals													
Tan2-RC5Ab*	44.0	4.27	9.10	11.9	0.43	5.74	7.91	8.89	3.85	2.79	0.280	0.161	98.9
Tan2-RC5Ba*	43.6	4.09	9.05	11.6	0.41	5.72	8.43	9.08	3.81	3.02	0.274	0.122	98.8
Tan2-RC5Bb*	43.9	3.93	9.04	12.0	0.43	5.96	8.52	9.45	3.88	3.13	0.286	0.127	100.2
Tan2-RC6c*	43.1	4.16	8.89	11.9	0.44	5.90	8.72	9.56	3.74	3.12	0.258	0.152	99.6
Average*	43.7	4.11	9.02	11.8	0.43	5.83	8.40	9.25	3.82	3.02	0.275	0.141	99.4
Standard													
VG2 (avg 6)	50.8	1.81	13.9	11.8	0.21	7.07	11.2	2.56	0.21	0.20	0.025	0.128	99.7

Averages of starred analyses excluding some that lost some Na_2O during weathering or analysis.

Table 5
Ar–Ar data on pegmatoid nepheline.

T (°C)	^{40}Ar (mol)	$^{40}Ar/^{39}Ar$	$^{37}Ar/^{39}Ar$	$^{36}Ar/^{39}Ar$	K/Ca	$\sum{}^{39}Ar$	$^{40}Ar^*$	Age (ka)
900	2.10E−14	0.1799	0.1603	0.0048	3.1	0.047	0.12	73 ± 2
1000	2.90E−14	0.1922	0.0724	0.0029	6.8	0.146	0.192	78 ± 1
1130	2.90E−14	0.1905	0.1536	0.0012	3.2	0.336	0.366	77 ± 1
1260	3.50E−14	0.1882	0.2119	0.0006	2.3	0.703	0.568	76 ± 1
1330	1.90E−14	0.1861	0.0508	0.0004	9.7	0.926	0.628	75 ± 1
1450	2.00E−14	0.1966	0.0473	0.0027	10	1	0.209	79 ± 1

Total fusion age, TFA = 76 ± 1 ka (including J).
Weighted mean plateau age, WMPA = 76 ± 1 ka (including J).
Inverse isochron age = 76 ± 2 ka. (MSWD = 0.87; $^{40}Ar/^{36}Ar = 277.6 \pm 1.6$).
Steps used: 900, 1000, 1130, 1260, 1330, 1450, (1–6/6 or 100% $\sum{}^{39}Ar$.
^{40}Ar (mol) = moles corrected for blank and reactor-produced ^{40}Ar.
$\sum{}^{39}Ar$ is cumulative, $^{40}Ar^*$ = rad fraction.
$J = 0.0002237$.

titanomagnetite. Therefore, variable abundance of melilite, in addition to element mobility discussed above, may modify the Sr content of a sample. This process is localized within the flow and is most likely caused by flow segregation since dark and light variants occur as adjacent bands, and are concentrated in the lower part of the flow. Most of the variant samples (MQ1D, MQ1L, MQ2, and GMQ12) have higher LREE/HREE than the flow mean (Fig. 9).

Unlike other HV lavas, Sugarloaf samples have crossing REE patterns in a PM-normalized plot (e.g., GMQ9 in Fig. 2). Such patterns are usually attributed to residual garnet during partial melting (Clague and Frey, 1982; Yang et al., 2003). In the thick Sugarloaf flow the lowermost sample GMQ12 has the highest La/Yb (Figs. 7a and 9), This may be evidence that the high LREE/HREE was caused by a process occurring as the flow was emplaced. Although

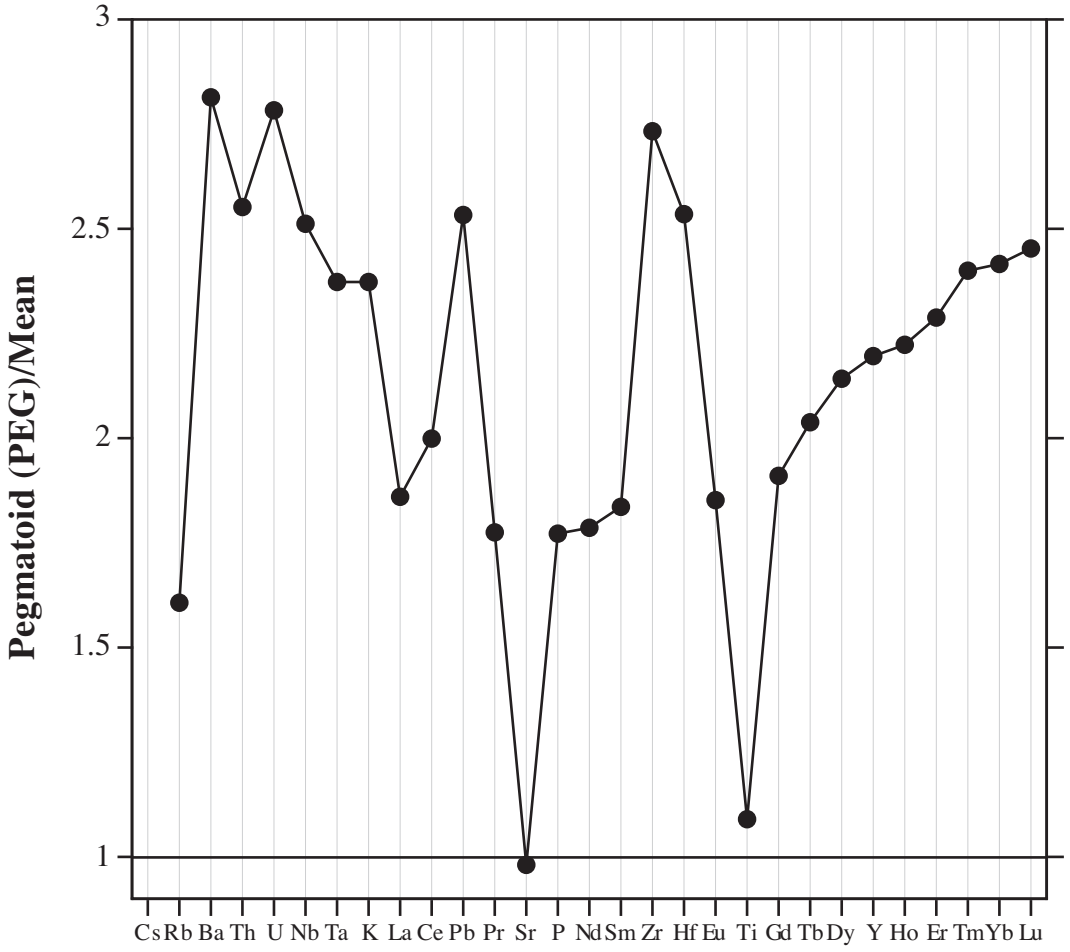

Fig. 10. Abundances of pegmatoid normalized to the mean of 12 main flow samples. The pegmatoid is strongly enriched in all incompatible elements except Sr and Ti. The HREE are more enriched than middle and light REE. The most enriched elements are Ba, Th, U, Pb, Zr, Hf, and the HREE.

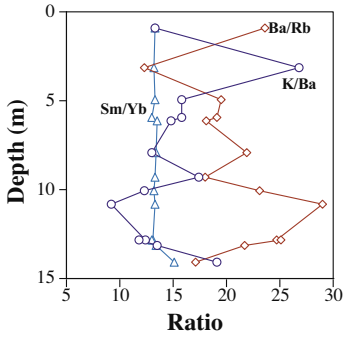

Fig. 11. Trace element ratios as a function of depth (in m) in the core. K/Ba and Ba/Rb have variable ratios compared with Sm/Yb, which is constant except at the base of the core.

we were unable to identify a mineral that would create high LREE/HREE, the pegmatodial segregations formed at low pressure have high HREE/LREE showing that complementary material to the pegmatoid would have low LREE/HREE. REE are moderately incompatible in melilite ($D^{melilite/melt}$ of 0.22 for Yb, 0.49 for Tb, and 0.61 for Sm; Nagasawa et al., 1980), so that unreasonably large amounts of melilite would have to be removed to fractionate REEs. Obviously such a process would affect melting models in terms of the amount of inferred residual garnet in the mantle.

5.2. Implications of flow heterogeneity produced during shallow processes on partial melting models

The key question in determining if the documented element mobility adversely affects the results of mantle melting models is: do the analyzed samples represent the composition of the magmas generated in the mantle or have post-melting surficial processes modified their compositions so much as to preclude inferences about the melting process? Clague and Frey (1982) used 65MOIL2 and Yang et al. (2003) used GMQ9 in their models. Both samples are in the group of 12 fine-grained samples that are thought to be representative of the bulk flow except for mobility of vapor-transported elements (Table 1). A different approach

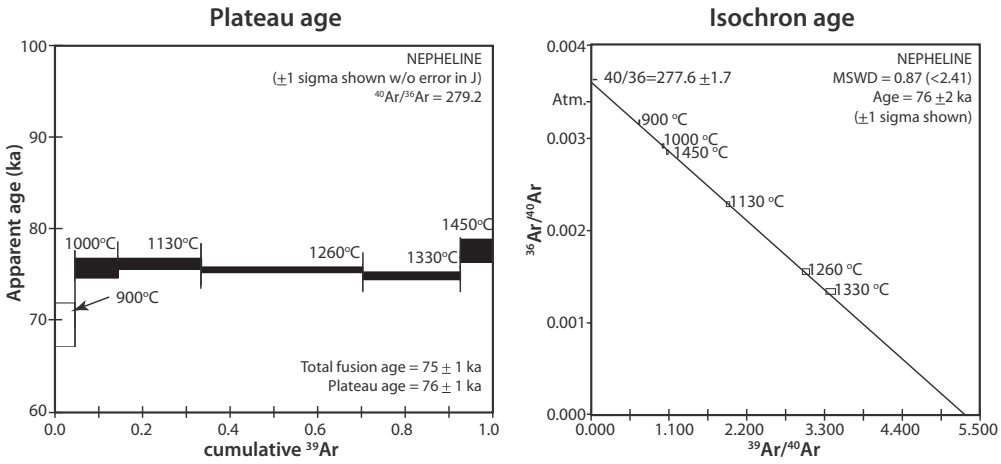

Fig. 12. Ar–Ar plateau and isochron plot of nepheline from a pegmatoid. Data from Table 5. Concordant plateau, isochron, and total fusion ages yield an age of 76 ± 1 ka. The isochron is tightly constrained and yields an atmospheric $^{40}Ar/^{36}Ar$ ratio of 277.6 ± 1.7.

is to estimate the relative percent of the flow that is aphanitic homogenous lava, pegmatoid, dark-colored and light colored variants and combine their compositions in the proper proportions to test if GMQ9 and 65MOIL2 are representative. The dark and light variants are almost exclusively in the lower portion of the flow where they represent a significant portion of the flow. Based on the proportions in the core and observed on the quarry face, we estimate that perhaps 15% of the bottom third of the flow consists of these variants (or ~5% of the total flow) and that the pegmatoids are probably no more than 2%. Combining the different types of lava that make up the flow in these proportions yields an average for the entire flow that is similar, but not identical, to the average of the 12 aphanitic main samples (Table 6), which in turn is similar to the analyses of GMQ9 and 65MOIL2. This exercise suggests that elements may migrate within the flow but that little is lost or gained and that the average of the 12 main samples is representative of the entire flow. The key lesson is that the composition of single samples may be misleading, but also that the two samples used in modeling the generation of the HV were representative (GMQ9 is better analyzed and therefore preferred) and the results of the results of modeling the mantle process are robust. The appropriateness of these two representative samples in the modeling was fortuitous and similar studies elsewhere would be well advised to analyze multiple samples from strongly alkalic lava flows, especially if the flow is visually heterogeneous.

The amount of residual garnet in the partial melting process that created the HV can be examined using Tb/Yb and Sc contents. The average Tb/Yb of 12 samples from the main flow is 1.35 whereas the variants range from 1.34 to 1.51 and the pegmatoid is 1.14. All these values are higher than the range of 0.5–0.8 for other HV flows (Yang et al., 2003). Likewise, Sc concentrations for the 12 main flow samples are 15.0 ± 0.6 ppm, the variants range from 12.9 to 14.5 ppm and the pegmatoid contains 39.5 ppm (Table 3). These concentrations compare to values of 18 –27 ppm (Clague and Frey, 1982) with an average of 24 for the remainder of the HV. Regardless of the percentages of the flow that consist of dark and light variants and pegmatoid, the Sugarloaf flow has anomalously low Sc and high Tb/Yb consistent with more garnet in the mantle residue than for other HV lavas. The high Tb/Yb and LREE/HREE are not unique to the Sugarloaf flow; the probably co-eruptive melilite nephelinite flows from the Rocky Hill and Tantalus vents (RH and HV02-19 in Fekiakova et al., 2007) share these characteristics.

Although the 19 samples of the Sugarloaf flow show significant intraflow heterogeneity in abundance of elements such as K that are mobile and in LREE/HREE, all samples of the HV have relative deficiencies in K and Ti compared to primitive mantle (see marked negative anomalies for K and Ti in Fig. 2) that reflect residual trace phases such as phlogopite, amphibole and Ti-oxides during partial melting (Clague and Frey, 1982; Yang et al., 2003). Although the pegmatoid segregations have created LREE/HREE variability within the Sugarloaf flow, this result does not affect the inference of more residual garnet causing the higher Tb/Yb in the Sugarloaf flow relative to other HV flows (Clague and Frey, 1982; Yang et al., 2003). We conclude that the modeling results of mantle melting to form the HV lavas (Clague and Frey, 1982; Yang et al., 2003) are unchanged by our improved understanding of element mobility within the strongly SiO_2-undersaturated Sugarloaf flow.

5.3. Eruption dynamics and flow emplacement

The ash produced during the eruptions along the Tantalus rift (Table 4) was deposited over a wide area, implying highly explosive activity (Stearns and Vaksvik, 1935). The petrography of the ash samples, with only small amounts of glass present, indicates that the erupted lavas had high crystal content. The interstitial glass and glass inclusions have high concentrations of Cl, unusually high S, and presumably other volatiles such as H_2O and CO_2.

Table 6
Bulk Sugarloaf flow reconstruction.

Sample	GMQ9	Mean of 12	Blend
SiO_2	37.67	37.80	37.87
TiO_2	2.84	2.89	2.89
Al_2O_3	10.26	10.74	10.76
FeO^*	15.98	16.10	16.06
MnO	0.24	0.25	0.25
MgO	11.77	11.84	11.77
CaO	13.31	12.46	12.44
Na_2O	4.95	4.82	4.84
K_2O	1.79	1.85	1.87
P_2O_5	1.20	1.24	1.26
Rb	49.0	48.8	49.2
Sr	1799	1830	1825
Ba	881	1042	1062
V	229	236	236
Ni	206	186	183
Zn	195	197	197
Ga	22.5	24.3	24.3
Y	22.4	25.5	25.8
Zr	237	274	279
Nb	79.0	93.7	95.5
Sc		16.3	16.6
Cr		300	296
Co		70.1	69.6
Hf		5.86	5.97
Ta		4.81	4.88
Th		8.74	8.88
La		74.9	75.7
Ce		157	158
Nd		71.4	72.0
Sm		15.6	15.8
Eu		5.02	5.07
Tb		1.60	1.62
Yb		1.20	1.22
Lu		0.15	0.16
Sr	1763	1767	1767
Sc	13.60	14.97	15.41
Rb	46.9	46.0	46.6
Zr	243	249	257
Y	25.8	26.2	26.8
Nb	85.9	88.9	91.7
Ba	925	925	962
La	71.10	71.7	72.8
Ce	144	148	151
Pr	18.0	18.0	18.3
Nd	73.8	72.1	73.2
Sm	14.9	15.0	15.2
Eu	4.61	4.56	4.63
Gd	11.8	12.1	12.4
Tb	1.49	1.52	1.55
Dy	6.37	6.44	6.58
Ho	0.94	0.94	0.96
Er	1.79	1.94	1.99
Tm	0.21	0.21	0.21
Yb	1.08	1.13	1.15
Lu	0.141	0.145	0.149
Hf	5.17	5.15	5.31
Ta	4.38	4.55	4.68
Pb	4.14	4.05	4.19
Th	7.80	7.74	7.97
U	2.10	2.01	2.09
Sr/Ce	12.2	12.0	11.8
Sr/Nd	23.9	24.5	24.3
Rb/La	0.66	0.64	0.64
Ba/La	13.0	12.9	13.1
Ba/Th	119	120	121

GMQ9 data from Yang et al. (2003) except Sc from Clague and Frey (1982).
Blend is 93% Mean of 12 + 5% Mean of Variants + 2% Pegmatoid.

Exsolution of these volatiles led to the vigorous fountaining that is inferred from the widespread distribution of the ash (Stearns and Vaksvik, 1935).

MELTS modeling (Ghiorso and Sack, 1995; Asimow and Ghiorso, 1998) failed to duplicate the observed crystallization sequence of olivine, titanomagnetite, and melilite as melilite did not appear in the models. A similar result, a lack of melilite in the crystallization products, was observed in high-pressure experiments by Tatsumi et al. (1999) using a melilite nephelinite sample from Hamada, southwest Japan. The experimental starting composition was similar to the average Sugarloaf flow, but with slightly lower MgO and FeO^* and higher CaO, Na_2O, K_2O, and P_2O_5. Their experiments at 1.05 to 2 GPa show liquidus temperatures of about 1260–1270 °C, similar to the results from our MELTS runs under varying P (1–5 kbar), fO_2 (FMQ to FMQ+2), and H_2O (0–2 wt%) contents for the average of 12 Sugarloaf samples. At liquidus temperatures similar to this, viscosity of the melt is only 0.3 Pascal seconds, consistent with the observed high flow rates of strongly SiO_2-undersaturated lava at Nyiragongo volcano in 1977 (Tazieff, 1977). The interstitial glass in the ash fragments, with an average of 6.3% MgO represent liquids at ~1130 °C with an estimated viscosity of the melt only of about 2 Pascal seconds. Addition of the >40% crystals would increase the viscosity by another order of magnitude. The composition of the intergranular glass in the ash samples suggest that the Sugarloaf flow, and perhaps other HV flows, erupted at temperatures more than 100 °C below their liquidus. Eruption of the highly crystalline, volatile-rich, viscous magma at low temperature could account for the emplacement of a 15-m thick flow of 'a' ā lava. Rowland and Walker (1990) proposed that a ā and pāhoehoe flows are produced during eruptions with high and low lava discharge rates, respectively. The compositional heterogeneity of the flow is caused by processes directly related to the thickness of the flow.

These inferred low eruption temperatures are in agreement with glass compositions of submarine HV samples from the west end of the Koko rift, the flank of Diamond Head, a cone on the northeast flank of the island, and a nephelinite from a canyon on the northeast side of O'ahu that have MgO contents between 4.6% and 7.5% (Clague et al., 2006). Glasses from subaerial Diamond Head have similar low eruption temperatures based on their low 6.4% MgO content (Pauly, 2011). Chemically similar lavas to those in the HV from the North Arch

Table 7
Ages of Honolulu Volcanics Vents (ka).

Stearns and Vaksvik (1935)	Modified Ozawa sequence	Gramlich et al. (1971)	Stearns and Dalyrmple (1978)	Lanphere and Dalrymple (1980)	Clague et al. (2006)	Ozawa et al. (2005)	This paper
Vent 8	1. Ha'iku					800 ka	
22	2. Maunawili					780	
4	3. Moku Manu					700	
3	4. Pyramid Rock					680	
14	5. Pali					620	
27	6. Kamanaiki					590	
16	7. Ka'au	650 ka				580	
23	8. Training School					580	
15	9. Mo kolea					580	
	T298 submarine cone				510 ka		
11	10. Kane'ohe					500	
17	11. Mau'umae			430 ka		480	
12	12. Luakaha	420		360		470	
19	13. Makalapa					470	
7	14. Kalihi	460		580		460	
1	15. Pu'u Hawai'iloa					430	
20	16. 'Ainoni					410	
18	Salt lake	430					
21	17. Castle	850				410	
28	18. Punchbowl	300		530		410	
2	19. Pali Kilo					400	
13	20. Makuku					400	
26	21. Black Point	300	410 ka	480		400	
	22. 'Akulikuli					390	
25	23. Kaimukı	284				380	
	T272-Diamond Head				360		
10	24. Aliamanu					250	
	25. Manoa					130	
36	26. Tantalus					100	
37	27. Mō'ili'ili	67				90	76 ka
9	28. Rocky Hill					50	
	T273-Koko Rift				100 ka		
34	29. Kaupo	32		320 ka		100	
33	30. Koko	40				100	
31	31. Kalama	34 ka				70	
Vent 32	32. Hanauma					70 ka	

(Clague et al., 1990; Yang et al., 2003) also have MgO contents of 5.7–10.25% and eruption temperatures significantly below that expected for primary melts. None of these HV or North Arch melt compositions have MgO contents (Clague and Frey, 1982; Dixon et al., 1997), or compositions of olivine phenocrysts (Frey et al., 2000), approaching those estimated for primary magma compositions of the HV or North Arch (Dixon et al., 1997). Although the rocks are near-primary in bulk composition, they are evolved melts carrying a cargo of crystals.

5.4. Age of the HV and hazards implications

The new age of the Sugarloaf flow of 76 ± 1 ka is compiled with prior ages determined for the HV in Table 7. The similarity of our new age to published ages of the Sugarloaf flow strengthens our confidence in the published ages. The Koko Rift, consisting of an offshore vent sampled by ROV dive D273 (Clague et al., 2006), and the Kaup-ō, Koko, Kalama, and Hanauma vents (Gramlich et al., 1971 and Ozawa et al., 2005), may be the youngest cluster of vents in the HV at ~35 ka (using an average of ages from Gramlich et al., 1971) with the Tantalus cluster consisting of Sugarloaf, Mānoa, and Rocky Hill, being older at ~76 ± 1 ka. Conversely, four Koko Rift samples dated by Ozawa et al. (2005) average 85 ka, which would make Koko Rift slightly older than the Tantalus Rift, as suggested by Stearns and Vaksvik (1935), Winchell (1947), and Macdonald et al. (1983). The older Koko Rift estimate would also suggest that the eruption frequency of the HV is longer than 35 ka and that there has been no activity in the last 76 ka. The 800 ka duration of the HV combined with the number of vent groups is consistent with a recurrence interval near the 35 ka estimated using the

Gramlich et al. (1971) Koko Rift age. This inferred sequence of eruptions and eruption frequency should be testable using new Ar–Ar dating techniques and lab equipment for samples from the Koko Rift. Whether the youngest HV eruptions were those forming the Tantalus or Koko Rifts, future eruptions of the HV remain possible.

6. CONCLUSIONS

The Sugarloaf flow has significant intraflow heterogeneity in major and trace element compositions. The variability in Na_2O, K_2O, CaO, Rb, Ba, U, Pb, and Sr is caused by late-stage vapor transport and deposition of zeolites and calcite. Segregation of pegmatoid also affects the composition of the remaining flow as does the formation of light-colored melilite-rich and dark-colored titanomagnetite-rich bands in the flow. Previous mantle melting models were based on samples that were fortuitously close to our estimated composition of the flow as a whole so their conclusions about the larger amount of garnet and presence of phlogopite, amphibole, and Fe–Ti oxides in the mantle residuum are therefore unchanged. The unusually thick flow resulted from a combination of high magma discharge rates, high fire fountains, and high viscosity of a magma erupted at least 100 °C below its liquidus temperature. The intraflow geochemical variability reflects processes of melt segregation and late stage volatile transport that were largely caused by the thickness of the flow and its apparent sluggish advance. The Sugarloaf flow erupted at 76 ± 1 ka from a cluster of vents that are likely the second youngest in the Honolulu Volcanics. With a possible 35–40 ka eruption frequency, the possibility of future eruptions cannot be precluded.

ACKNOWLEDGEMENTS

This study was begun in the early 1980s as an attempt to evaluate the severity of element mobility on several scales within the thick Sugarloaf flow. The study was initiated by Fred Frey, who was deeply concerned that intraflow variability caused by post-eruptive processes might compromise the conclusions reached by modeling the process of mantle melting. Its completion is a tribute to Fred, who never wavered in developing and testing ideas about the formation of the range of basalts erupted on Earth. We thank the many analysts listed in the text, who should be pleased that their labors provided the basis for this study, and Charles Langmuir for access to his lab at Harvard and Zhongxing Chen for help with ICP-MS measurements when we decided to modernize our trace element data set. Brian Dreyer assisted with exploring the Sugarloaf composition within the MELTS program. Alicia Presti determined the modes for the core. NSF grant to MG (EAR-1219955) supported work on this project.

APPENDIX 1

Microprobe mineral compositions for sample 79MOIL-1 and melilite in Tantalus ash.

Flow	Ol-c	Ol-r	Cpx-c	Cpx-r	Cpx-c	Cpx-r	Mel-c	Mel-r	Neph	Timag-lg	Timag-sm	Perovskite
SiO_2	39.1	38.8	49.4	50	50.4	48	41.7	41.7	41.9 ± 0.2			
TiO_2			2.3	2	1.8	2.9	0.1	0.1		17.8–20.9	16.6	26.6–27.0
Al_2O_3			2.7	2	2	3.7	7.7	6.3	33.9 ± 0/2	2.1–0.7	1.4	0.1
FeO	17.2	19	6.4	6.2	5.9	6.9	3.4	4.7		71.6–69.8	70.2	57.8–57.1
MnO	0.16	0.42	0.2	0.1	0.1	0.1	0	0.1		0.8	0.7	0.75
MgO	43.5	41.9	14.3	14.6	14.6	13.7	8	7.5		2.9–2.6	5.2	1.35
CaO	0.2	0.64	23.5	23.4	23.7	23.4	32.9	31.9	0.04 ± 0.1			
Na_2O			0.8	0.7	0.6	0.9	4.4	4.6	16.8 ± 0.1			4.9–4.5
K_2O							0.1	0.1	7.1 ± 0.1			
SrO							1	2.8				
Total	100.2	100.8	99.6	99	99.1	99.6	99.4	99.8	99.74	95.2–94.8	94.1	91.5–90.8
Pegmatoid			Cpx-c	Cpx-rim	Cpx-c	Cpx-r	Mel-c	Mel-r	Neph	Ash-Mel		
SiO_2			51.2	51.7	48.7	49.6	43.7	43.6	42.7 ± 0.1	43.45		
TiO_2			1.5	1.2	2.4	2.3	0.1	0		0.1		
Al_2O_3			0.9	0.6	2.1	1.4	6.2	6.25	33.5 ± 0.1	7.66		
FeO			6.8	7.5	6.6	7.8	3.7	4.4		2.95		
MnO			0.2	0.2	0.1	0.1	0	0.1		0.05		
MgO			14.4	14	14.4	13.3	8.1	7.65		7.96		
CaO			23.7	23.4	23.7	22.9	33.1	32.9	0.22 ± 0.01	34.91		
Na_2O			0.7	0.8	0.8	1.1	4	4.4	16.1 ± 0.1	3.71		
K_2O							0.1	0.1	7.3 ± 0.2	0.13		
SrO							0.9	0.9				
Total			99.4	99.4	98.8	98.5	99.9	100.3	99.82	100.8		

Ol = olivine, Cpx = clinopyroxene, Mel = melilitite, Neph = nepheline, Timag = titanomagnetite, c-core, r-rim, lg = large, sm-small hexagon.

Analyses done at University of Hawaii except the melilite in TAN2 ash done at US Geological Survey in Menlo Park, CA.

REFERENCES

Asimow P. D. and Ghiorso M. S. (1998) Algorithmic modifications extending MELTS to calculate subsolidus phase relations. *Am. Mineral.* **83**, 1127–1131.

Clague D. A. and Frey F. A. (1982) Petrology and trace element geochemistry of the Honolulu Volcanics, Oahu: implications for the oceanic mantle below Hawaii. *J. Petrol.* **23**(447–504).

Clague D. A., Holcomb R. T., Sinton J. M., Detrick R. S. and Torresan M. E. (1990) Pliocene and Pleistocene alkalic flood basalts on the seafloor north of the Hawaiian Islands. *Earth Planet. Sci. Lett.* **98**, 175–191.

Clague D. A., Paduan J. B., McIntosh W. C., Cousens B. L., Davis A. S. and Reynolds J. R. (2006) A submarine perspective of the Honolulu Volcanics, Oahu. *J. Volcanol. Geotherm. Res.* **151**, 279–307.

Class C. and Goldstein S. L. (1997) Plume-lithosphrre interactions in the ocean basins: constraints from the source mineraology. *Earth Planet. Sci. Lett.* **156**, 245–260.

Cross, W. (1915) Lavas of Hawaii and their relations. Prof. Paper. U.S. Geol. Surv. 88.

Dana, J.D. (1849) United States Exploring Expedition During the Years 1838, 1839, 1840, 1841, 1842, New York, George P. Putnam, 756 p.

Davis A. S., Clague D. A. and Friesen W. B. (1994) Petrology and mineral chemistry of basalt from the Escanaba Trough, southern Gorda Ridge. *U.S. Geol. Surv. Bull.* **2022**, 153–170.

Dixon J. E., Clague D. A., Wallace P. and Poreda R. (1997) Volatiles in alkalic basalts from the North Arch Volcanic Field, Hawaii: extensive degassing of deep submarine-erupted alkalic series lavas. *J. Petrol.* **38**, 911–939.

Dunham K. C. (1933) Crystal cavities in lavas from the Hawaiian Islands. *Am. Mineral.* **18**, 369–385.

Dutton, C.E. (1884) Hawaiian volcanoes, U.S. Geol. Survey 4th Annual Report, 75-219.

Fekiakova Z., Abouchami W., Galar S. J. G., Garcia M. O. and Hofmann A. W. (2007) Origin and temporal evolution of Ko'olau Volcano, Hawaiì: Inferences from isotope data on the Ko1olau Scientific Drilling Project (KSDP), the Honolulu Volcanics and ODP Site 843. *Earth Planet. Sci. Lett.* **261**, 65–83.

Frey F. A., Green D. H. and Roy S. D. (1978) Integrated models of basalt petrogenesis: a study of quartz tholeiites to olivine melilitites from southeastern Australia utilizing geochemical and experimental petrological data. *J. Petrol.* **19**, 463–513.

Frey F. A., Clague D. A., Mahoney J. and Sinton J. (2000) Volcanism at the edge of the Hawaiian plume: petrogenesis of submarine alkalic lavas from the North Arch Volcanic Field. *J. Petrol.* **41**, 667–691.

Fitton J. G. and Hughes D. J. (1981) Strontian melilite in a nephelinite lava from Etinde, Cameroon. *Mineral. Mag.* **44**, 261–2641.

Gast P. W. (1968) Trace element fractionation and the origin of tholeiitic and alkalic magma types. *Geochem. Cosmochim. Acta* **32**, 1057–1086.

Gramlich J. W., Lewis V. A. and Naughton J. J. (1971) Potassium-argon dating of Holocene basalts of the Honolulu Volcanic Series. *Geol. Soc. Am. Bull.* **82**, 1399–1404.

Ghiorso M. S. and Sack R. O. (1995) Chemical mass transfer in magmatic processes. IV. A revised and internally consistent thermodynamic model for the interpolation and extrapolation of liquid-solid equilibria in magmatic systems at elevated temperatures and pressures. *Contrib. Miner. Petrol.* **119**, 197–212.

Hitchcock C. H. (1900) Geology of Oahu. *Geol. Soc. Am. Bull.* **11**, 15–60.

Hofmann A. W. (2004) Sampling mantle heterogeneity through oceanic basalts: isotopes and trace elements. In *Treatise of Geochemsitry* (eds. R. W. Carlson, H. D. Holland and K. K. Turekian). Elsevier, Oxford, pp. 61–101.

Huang S., Vollinger M.J., Frey F.A., Rhodes J.M. and Zhang Q. (2016) Compositional variation within thick (>10 m) flow units of Mauna Kea Volcano cored by the Hawaii Scientific Drilling Project. *Geochim. Cosmochim. Acta*. **185**, 182–197.

Ila, P., and Frey, F.A. (1984) Utilization of neutron activation analysis in the study of geologic materials, in Use and Development of Low and Medium Flux Research Reactors (eds. O.K. Harling, L. Clark and P. von der Hardt) supplement to vol. 44 Atomkernenergie Kerntechnik, 710-716.

Jackson E. D. and Wright T. L. (1970) Xenoliths in the Honolulu Volcanic Series, Hawaii. *J. Petrol.* **1**, 405–430.

Johnson K. T. M. (1998) Experimental determination of partition coefficients for rare earth and high-field strength elements between clinopyroxene, garnet, and basaltic melt at high pressures. *Contrib. Mineral. Petrol.* **133**, 60–68.

Laj C., Szeremeta N., Kissel C. and Guillou H. (2000) Geomagnetic paleointensities in Hawaii between 3.9 and 2.1 Ma: preliminary results. *Earth Planet. Sci. Lett.* **179**, 191–204.

Lanphere M. A. and Dalrymple G. B. (1980) Age and strontium isotopic composition of the Honolulu Volcanic Series, O'ahu, Hawaii. *Am. J. Sci.* **280-A**, 736–751.

Macdonald G. A., Abbott A. T. and Cox D. C. (1983) *Volcanoes in the sea*. University of Hawaii Press, Honolulu, 517 p.

McDonough W. F. and Sun S. S. (1995) The composition of the Earth. *Chem. Geol.* **120**, 223–263.

McMurtry G. M., Campbell J. F., Fryer G. L. and Fietzke J. (2010) Uplift of Oahu, Hawaii, during the past 500 k. y., as recoded by elevated reef deposits. *Geology* **38**, 27–30.

Nagasawa H., Schreiber H. D. and Morris R. V. (1980) Experimental mineral/liquid partitions coefficients of the rare earth elements (REE), Sc, and Sr for perovskite, spinel, and melilite. *Earth Planet. Sci. Lett.* **46**, 431–437.

Ozawa A., Ragami T. and Garcia M. O. (2005) Unspiked K-Ar dating of the Honolulu rejuvenated and Koolau shield volcanism on Oahu, Hawaiì. *Earth Planet. Sci. Lett.* **232**, 1–11.

Pauly, B. D. (2011) In situ micro-analytical investigations of palagonitization. Ph.D. dissertation, 1779 pp., Univ. of Calif., Davis, Calif.

Philpotts J. A., Schnetzler C. C. and Thomas H. M. (1972) Petrogenetic implications of some new geochemical data on eclogite and ultrabasic inclusions. *Geochem. Cosmochim. Acta* **36**, 1131–1166.

Roden M. F., Frey F. A. and Clague D. A. (1984) Geochemistry of tholeiitic and alkalic lavas fro the Koolau Range, Oahu, Hawaii: implications for Hawaiian volcanism. *Earth Planet. Sci. Lett.* **69**, 141–158.

Rowland S. K. and Walker G. P. L. (1990) Pahoehoe and aa in Hawaii: volumetric flow rate controls lava structure. *Bull. Volcanol.* **52**, 615–628.

Schilling J. G. and Winchester J. W. (1969) Rare-earth contribution to the origin of Hawaiian lavas. *Contrib. Mineral. Petrol.* **23**, 27–37.

Stearns H. T. (1940) Supplement to the geology and groundwater resources of the island of Oahu, Hawaii. *Bull Hawaii Div. Hydrography* **5**, 1–164.

Stearns, H.T., and Dalyrmple, G.B. (1978) The K-Ar age of the Black Point dike on Oahu, Hawaii, and its relation to the Yarmount interglaciation, Occ. Papers of the B.P. Bishop Museum, XXIV, 307-313.

Stearns H. T. and Vaksvik K. N. (1935) Geology and groundwater resources of the island of O'ahu. *Hawaii Bull. Hawaii Div. Hydrography* **1**, 1–479.

Stearns H. T. and Vaksvik K. N. (1938) Records of the drilled wells on Oahu, Hawaii. *Bull. Hawaii Div. Hydrography* **4**, 1–213.

Taggart, J.E., Jr., Lindsay, J.R., Scott, B.A., Vivit, D.V., Bartel, A. J., and Stewart, K.C. (1987) Analysis of geological materials by wavelength-dispersive X-ray fluorescence spectro- metry. In: Baedecker, P. H. (ed.) Methods for Geochtmical Analysis. US Geological Survty Bulletin, 1170, E1–E19.

Tatsumi Y., Arai R. and Ishizaka K. (1999) The petrology of a melilite-olivine nephelinite from Hamada, SW Japan. *J. Petrol.* **40**, 497–509.

Tazieff H. (1977) An exceptional eruption: Mt. Nyiragongo, Jan. 10, 1977. *Bull. Volcanol.* **30**, 189–200.

Tedesco D., Vaselli O., Papale P., Carn S. A., Voltaggio M., Sawyer G. M., Dureieux J. and Kasereka M. (2007) January 2002 volano-tectonic eruption of Nyiragongo Volcano, Democratic Republic of Congo. *J. Geophys. Res.* **112**, 2156–2202. http://dx.doi.org/10.1029/2006JB004762.

Tilley, C.E., Yoder, H.S. Jr., Schairer, J.F. (1965) Melting relations of volcanic tholeiitic and alkalic rock series, Year Book-Carnegie Institution of Washington, 69-82.

Wilkinson J. F. G. and Stolz A. J. (1983) Low-pressure fractionation of strongly undersaturated alkaline ultrabasic magma: the olivine-melilite-nephelinite at Moiliili, Oahu, Hawaii. *Contrib. Mineral. Petrol.* **83**, 363–374.

Winchell H. (1947) Honolulu Series, Oahu, Hawaii. *Bull. Geol. Soc. Am.* **58**, 1–48.

Yamasaki S., Sawada R., Ozawa A., Tagami T. and Watanabe Y. (2011) Unspiked K–Ar dating of Koolau lavas: Evaluation of the influence of weathering/alteration on age determinations. *Chem. Geol.* **257**, 41–53.

Yang H.-J., Frey F. A. and Clague D. A. (2003) Constraints on the source components of lavas forming the Hawaiian North Arch and Honolulu Volcanics. *J. Petrol.* **44**, 603–627.

Associate editor: Marc Norman